

1 **Global analysis of cell behavior and protein localization dynamics**
2 **reveals region-specific functions for Shroom3 and N-cadherin during**
3 **neural tube closure.**

4

5 **Austin T. Baldwin, Juliana Kim, and John B. Wallingford***

6

7 Dept. of Molecular Biosciences, University of Texas at Austin

8

9

10

11

12

13

14 *Corresponding author

15 Wallingford@austin.utexas.edu

16 Patterson Labs

17 2401 Speedway

18 Austin, TX. 78751

19 Wallingford@austin.utexas.edu

1 **Abstract**

2 Failures of neural tube closure are common and serious birth defects, yet we have a poor
3 understanding of the interaction of genetics and cell biology during neural tube closure.
4 Additionally, mutations that cause neural tube defects (NTDs) tend to affect anterior or posterior
5 regions of the neural tube but rarely both, indicating a regional specificity to NTD genetics. To
6 better understand the regional specificity of cell behaviors during neural tube closure, we
7 analyzed the dynamic localization of actin and N-cadherin via high-resolution tissue-level time-
8 lapse microscopy during *Xenopus* neural tube closure. To investigate the regionality of gene
9 function, we generated mosaic mutations in *shroom3*, a key regulator of neural tube closure
10 This approach elucidates new differences between cell behaviors during cranial/anterior and
11 spinal/posterior neural tube closure, provides mechanistic insight into the function of *shroom3*
12 and demonstrates the ability of tissue-level imaging and analysis to generate cell-biological
13 mechanistic insights into neural tube closure.

14

15 **Introduction:**

16 Congenital birth defects are the number one biological cause of death for children in the US,
17 and neural tube defects (NTDs) represent the second most common class of human birth defect
18 (Murphy et al., 2018; Wallingford et al., 2013). NTDs represent a highly heterogeneous group of
19 congenital defects in which failure of the neural folds to elevate or fuse results in a failure of the
20 skull or spine to enclose the central nervous system (Wallingford et al., 2013). While genetic
21 analyses in both humans and animal models have revealed dozens of genes necessary for
22 normal neural tube closure, several key questions remain.

23 One central unanswered question relates to the regional heterogeneity of both normal neural
24 tube closure and pathological NTDs. For example, the collective cell movements of convergent
25 extension dramatically elongate the hindbrain and spinal cord of vertebrates, but not the
26 midbrain and forebrain (Nikolopoulou et al., 2017; Wallingford et al., 2013). Accordingly,
27 disruption of genetic regulators of convergent extension such as the Planar Cell Polarity (PCP)
28 genes results in failure of neural tube closure in posterior regions of the neural ectoderm, but
29 not anterior (Kibar et al., 2001; Wang et al., 2006). Conversely, the *Shroom3* gene is implicated
30 in apical constriction, a distinct cell behavior that drives epithelial sheet bending, and disruption
31 of *shroom3* elicits highly penetrant defects in anterior neural tube closure, but only weakly
32 penetrant defects in the posterior (Haigo et al., 2003; Hildebrand and Soriano, 1999). This
33 regional deployment of apical constriction in the anterior and convergent extension in the
34 posterior during neural tube closure is poorly understood.

35 In addition, the underlying mechanisms of individual cell behaviors necessary for neural tube
36 closure remain incompletely defined. While apical constriction is driven by actomyosin
37 contraction, the precise site of actomyosin action during this process is unclear and constitutes
38 a long-term problem in the field (Martin and Goldstein, 2014). For example, analysis of apical
39 constriction during gastrulation in both *Drosophila* and *C. elegans* has shown integration of
40 discrete junctional and medio-apical (“medial”) populations of actomyosin (Coravos and Martin,
41 2016; Martin et al., 2009; Roh-Johnson et al., 2012). Recent studies in frog and chick embryos
42 have also described similar pulsed medial actomyosin-based contractions occurring during
43 neural tube closure (Brown and García-García, 2018; Christodoulou and Skourides, 2015;

1 Suzuki et al., 2017), but how those contractions are controlled and how they contribute to cell
2 shape change during neural tube closure are not known.

3 For example, Shroom3 is among the more well-defined regulators of apical constriction, being
4 both necessary and sufficient to drive this cell shape change in a variety of cell types, including
5 the closing neural tube (Haigo et al., 2003; Hildebrand, 2005; Plageman et al., 2010; Plageman
6 et al., 2011b). Shroom3 is known to act via Rho Kinase to drive apical actin assembly and
7 myosin contraction (Das et al., 2014; Hildebrand, 2005; Nishimura and Takeichi, 2008;
8 Plageman et al., 2011a). However, the relationships between Shroom3, and the medial and
9 junctional populations of actin have not been explored.

10 An additional outstanding question relates to the interplay of actomyosin contractility and cell
11 adhesion during apical constriction. The classical cadherin Cdh2 (N-cadherin) is essential for
12 apical constriction during neural tube closure in *Xenopus* (Morita et al., 2010; Nandadasa et al.,
13 2009), and *shroom3* displays robust genetic interactions with *n-cadherin* in multiple
14 developmental processes, including neural tube closure (Plageman et al., 2011b). Moreover, a
15 dominant-negative N-cadherin can disrupt the ability of ectopically-expressed Shroom3 to
16 induce apical constriction in MDCK cells (Lang et al., 2014). Nonetheless, it is unclear if or how
17 Shroom3 controls the interplay of N-cadherin and actomyosin during apical constriction. This is
18 an important gap in our knowledge, because despite the tacit assumption that cadherins interact
19 with each other and control actomyosin at cell-cell junctions, N-cadherin displays multiple cell-
20 autonomous activities (Rebman et al., 2016; Sabatini et al., 2011). Intriguingly, several papers
21 now demonstrate that extra-junctional cadherins at free cell membranes can engage and
22 regulate the actomyosin cortex (Ichikawa et al., 2020; Padmanabhan et al., 2017; Sako et al.,
23 1998; Wu et al., 2015).

24 Finally, though Shroom3 has been extensively studied in the context of apical constriction,
25 recent studies also implicate Shroom family proteins in the control of convergent extension
26 (McGreevy et al., 2015; Nishimura and Takeichi, 2008; Simões Sde et al., 2014). Several
27 studies indicate a genetic and cell biological interplay of Shroom3 and the PCP proteins (Durbin
28 et al., 2020; McGreevy et al., 2015), and one study directly links PCP, apical constriction and
29 convergent extension (Nishimura et al., 2012). Conversely, some studies also suggest a role
30 for PCP proteins in apical constriction (Ossipova et al., 2015). Given the better-understood role
31 of PCP in regulating convergent extension in the posterior neural ectoderm, how Shroom3
32 controls convergent extension and PCP in the posterior remains especially unclear.

33 Together, these studies highlight the complexity of neural tube closure, which is compounded by
34 the sheer scale of the tissue involved. The neural ectoderm is comprised of hundreds to
35 thousands of cells (depending on organism) and stretches from the anterior to posterior poles of
36 the developing embryo. However, the vast majority of dynamic studies of cell behavior in the
37 neural tube closure, including our own, have focused on small numbers of cells due to
38 constraints of both imaging and image analysis.

39 Here, we used image-tiling time-lapse confocal microscopy to obtain over 500,000 individual
40 measurements of cell behaviors associated with neural tube closure in *Xenopus tropicalis*.
41 Using these data, we demonstrate that the cell biological basis of apical constriction differs
42 substantially between the anterior and the posterior neural plate. Second, we demonstrate that
43 the crux of Shroom3 function lies not in actin assembly *per se*, but rather in the coupling of actin
44 contraction to effective cell shape change. Third, we demonstrate that the control of N-cadherin

1 localization is also a key feature of Shroom3 function during neural tube closure. Finally, we
2 demonstrate that the incompletely penetrant posterior phenotype of *shroom3* mutants also
3 results from dysregulation of both actin and N-cadherin localization. Overall, these findings a)
4 elucidate differences between cell behaviors during cranial/anterior and spinal/posterior neural
5 tube closure, b) provide mechanistic insight into the function of *shroom3*, an essential neural
6 tube closure gene, and c) demonstrate the ability of tissue-level imaging and analysis to
7 generate cell-biological mechanistic insights into neural tube closure.

8

9

10 **Results and Discussion:**

11

12 **High-content imaging of cell behavior and protein localization during vertebrate neural** 13 **tube closure**

14 *Xenopus tropicalis* affords several advantages for imaging neural tube closure, as its cells are
15 large and easily accessible; its culture conditions for imaging are no more complex than
16 synthetic pond water held at room temperature; and its broad molecular manipulability allows
17 examination of diverse fluorescent markers. We used confocal microscopy and image tiling to
18 collect high-magnification datasets spanning broad regions of the folding neural ectoderm from
19 embryos injected at blastula stages with mRNAs encoding fluorescent reporters (**Fig. 1A**). At
20 the onset of neurulation, embryos were positioned to image either the anterior (roughly
21 corresponding to the brain) or the more posterior (roughly corresponding to the spine) regions of
22 the neural ectoderm. Cells captured in the resulting movies were then segmented using Tissue
23 Analyzer and CSML (Aigouy et al., 2016; Ota et al., 2018), yielding a map of both the apical cell
24 surfaces and all individual junctions (**Fig. 1B**). Using Tissue Analyzer (Aigouy et al., 2010;
25 Aigouy et al., 2016) and Fiji (Schindelin et al., 2012), we quantified both cell behaviors and the
26 localization of fluorescent protein reporters.

27 Actomyosin contractility is the key driver of apical constriction, so we labeled actin using LifeAct-
28 RFP (Riedl et al., 2008) to quantify actin localization (**Fig. 1A, magenta**). Because previous
29 studies suggest that distinct actomyosin populations at the medial apical surface and the apical
30 cell junctions play distinct roles in apical constriction (Coravos and Martin, 2016; Martin et al.,
31 2009; Roh-Johnson et al., 2012), we quantified these populations separately (**Fig. 1C, D**).
32 Because cell adhesion is also essential for epithelial morphogenesis and N-cadherin is essential
33 for neural tube closure in *Xenopus* (Nandadasa et al., 2009), we co-labeled cells with N-
34 cadherin-GFP (**Fig. 1A, green**).

35 In total, our dataset is comprised of ~190,000 observations of apical cell surfaces from over
36 3000 cells and ~450,000 observations from over 10,000 individual cell-cell junctions (**Fig. 1D,**
37 **E**), collected at a rate of one frame/observation per minute over 1-2 hours across seven
38 embryos spanning roughly stages 13 to 18 (Nieuwkoop and Faber, 1994).

39 As an initial test of the validity of our approach, we examined our dataset for well-known trends
40 expected for neural epithelial cells during neural tube closure, namely an overall decrease in
41 apical area and an overall increase in apical actin intensity. The heat maps in **Fig. 2A and B**
42 reveal that cells in both anterior and posterior regions generally reduce their apical surface area

1 and increase medial actin intensity, as expected. These overall trends are backed by
2 examination of individual cells, as shown for specific representative cells in **Fig. 2C**. Overall,
3 this analysis suggests that our pipeline is generally effective for quantifying cell shape and actin
4 intensity in over time during neural tube closure.

5

6 **Distinct patterns of behavior drive apical constriction in the anterior and posterior** 7 **regions of the neural plate during neural tube closure.**

8 The incidence and form of NTDs differ between the brain and spinal cord in both humans and
9 mouse genetic models (Nikolopoulou et al., 2017; Wallingford et al., 2013), yet how the
10 dynamics of individual cell behaviors differ between the anterior and posterior regions remains
11 poorly defined. We therefore quantified the temporal progression of apical constriction between
12 the two regions, and we observed consistent and significant differences.

13 As noted above, bulk measurements show a decrease in apical area in both regions over time
14 (**Fig. 3A**). However, we observed distinct region-specific distributions for these changes. For
15 example, a significantly higher proportion of anterior cells displayed significant apical
16 constriction as compared to cells of the posterior region (**Fig. 3A**). We also observed
17 differences in the timing of constrictions, with anterior cells displaying a more gradual reduction
18 in apical area across the period of observation, while cells in the posterior display late, rapid
19 reductions in apical area (**Fig. 3A'**).

20 Medial and junctional actin intensity also generally increased over time in both regions, with
21 their temporal progressions reflecting the changes in apical area described above (**Fig. 3B, B',**
22 **C, C'**). Likewise, the distributions of changes in both medial and junctional actin were
23 significantly different between the two regions, with cells in the spine having a significantly more
24 heterogeneous distribution of actin accumulation outcomes (**Figure 3B, C**).

25 Most intriguing were the dynamics of N-cadherin localization, for which we observed two
26 surprising patterns. First, in the anterior neural ectoderm we noticed that not only junctional *but*
27 *also medial* N-cadherin dynamics strongly reflected those observed for actin (**Fig. 3D, D', E, E'**).
28 The latter result was surprising because classical cadherins such as N-cadherin are typically
29 known for their function at apical cell-cell junctions. However, a new understanding of the cell-
30 autonomous functions of cadherins, including N-cadherin, is now emerging (Ichikawa et al.,
31 2020; Rebman et al., 2016; Sabatini et al., 2011). Indeed, so-called “extra-junctional cadherins”
32 have been shown to interact with and even regulate the actomyosin cortex in cultured cells and
33 *C. elegans* embryos (Padmanabhan et al., 2017; Sako et al., 1998; Wu et al., 2015). Our result
34 suggests another noncanonical, non-junctional function for N-cadherin in the vertebrate neural
35 plate.

36 In contrast to these patterns in the anterior neural ectoderm, N-cadherin dynamics in the
37 posterior did *not* closely reflect actin dynamics. Though the pattern of actin accumulation in
38 posterior neural ectoderm cells was more heterogeneous than that observed anteriorly, a
39 majority of cells in the posterior plate accumulated both junctional and apical actin (**Fig. 3B, C**).
40 However, neither junctional nor medial N-cadherin displayed significant accumulation in the
41 posterior neural plate during the period of observation (**Fig. 3D, E**). These data provide a
42 quantitative description of actin and N-cadherin dynamics in the developing neural plate and

1 suggest that distinct mechanisms link actomyosin and cell adhesion to cell shape change in the
2 anterior and posterior regions of the developing vertebrate neural ectoderm.

3

4 **Mosaic mutation of *shroom3* reveals distinct anterior and posterior phenotypes in the** 5 **neural ectoderm.**

6 The differences in cell behaviors observed between anterior and posterior neural ectodermal
7 regions mirrored the region-specific nature of NTDs in both humans and animal models. We
8 therefore sought to understand how specific changes in cell behavior may explain region-
9 specific NTDs. To this end, we examined the function of the *shroom3* gene, which is implicated
10 in human NTDs and has variably penetrant effects on anterior and posterior neural tube closure,
11 with more severe and penetrant anterior defects being observed in both mice and *Xenopus*
12 (Deshwar et al., 2020; Haigo et al., 2003; Hildebrand and Soriano, 1999; Lemay et al., 2015).

13 F0 mutagenesis using CRISPR has recently emerged as a powerful tool in *Xenopus* and
14 zebrafish, and mosaic crispants generated by targeted injections allow simultaneous
15 observation of wild-type and crispant cellular phenotypes so that observations are automatically
16 staged and synchronized (Aslan et al., 2017; Kakebeen et al., 2020; Kroll et al., 2021; Szenker-
17 Ravi et al., 2018; Willsey et al., 2020). We therefore designed sgRNAs that effectively targeted
18 the *shroom3* locus in *X. tropicalis* (**Methods Appendix Figure 1A, B**). Injection of these
19 sgRNAs together with Cas9 protein into the 2 dorsal-animal blastomeres at the 8-cell stage
20 induced neural tube closure defects (**Methods Appendix Figure 1C, D**), thus recapitulating
21 knockdowns in *Xenopus* using MOs (Haigo et al., 2003), as well as the results in mouse genetic
22 mutants (Hildebrand and Soriano, 1999). Critically, injections of sgRNA without Cas9 had no
23 effect (**Methods Appendix Figure 1C, D**).

24 We therefore labeled the neural plate by injection of fluorescent reporters into both dorsal
25 blastomeres at the 4-cell stage, and then injected a mixture of *shroom3*-targeted sgRNA, Cas9
26 protein, and membrane-BFP mRNA into one dorsal blastomere of 8-cell stage embryos to
27 generate mosaic crispants (**Fig. 4A and see Methods Appendix Figure 1**), in which we identify
28 *shroom3* crispant cells via membrane-BFP localization (**Fig. 4B**). Maps of the initial
29 conformations of our imaged embryos and their *shroom3* crispant cell calls are located in
30 **Methods Appendix Figure 2**. These maps allow us to systematically assess the relative
31 locations of control and *shroom3* crispant cells along mosaic interfaces. For the purposes of
32 brevity and simplicity, in this study we have not included in our analyses any cells or cell
33 junctions situated along the mosaic interface (i.e. control cells that had *shroom3* crispant
34 neighbors, *shroom3* crispant cells that had control neighbors, or junctions between control and
35 *shroom3* crispant cells).

36 Importantly, this F0 CRISPR-based approach recapitulated the known, specific cell biological
37 phenotype of *Shroom3* loss, as demonstrated previously in the neural tube of *Xenopus*
38 morphants and mouse mutants (Lee et al., 2007; McGreevy et al., 2015; Plageman et al., 2010).
39 Specifically, we observed a gross failure of anterior neural tube closure associated with
40 defective apical constriction (**Fig. 4**). In the anterior region, *shroom3* crispant cells displayed
41 significantly enlarged apical surfaces at the onset of our imaging (~st. 13), and this phenotype
42 grew more severe over time (**Fig. 4C, left**). Cells in the posterior region displayed a far more
43 subtle phenotype, and while these cells were less constricted than controls at the onset of
44 imaging, this phenotype did not become more severe over time (**Fig. 4C, right**). Thus, the

1 change in apical area over the course of imaging was significantly disrupted in cells of the
2 anterior neural plate, but surprisingly, was not significantly disrupted in the posterior neural plate
3 during the period of imaging (**Fig. 4D**).

4 In summary, our F0 mosaic mutagenesis of *shroom3* elicited apical constriction phenotypes
5 across the neural ectoderm, but the phenotype was far stronger in the anterior, consistent with
6 the gross phenotype of highly penetrant anterior NTDs and far less penetrant posterior NTDs in
7 both frog and mouse embryos lacking Shroom3 function (Haigo et al., 2003; Hildebrand and
8 Soriano, 1999; McGreevy et al., 2015).

9

10 **Shroom3 links actin dynamics to effective apical constriction in the anterior neural** 11 **ectoderm.**

12 A unified mechanism for apical constriction has emerged in recent years whereby apical
13 constriction is driven by two discrete populations of actomyosin positioned either at apical cell-
14 cell junctions or the medial apical cell surface (Martin and Goldstein, 2014). However, this
15 model has been developed from studies in *C. elegans* and *Drosophila*, and the extent to which
16 the model applies in vertebrates is unknown. We therefore examined our time-lapse data from
17 the anterior neural ectoderm in order to understand the interplay of junctional and medial actin
18 dynamics during vertebrate apical constriction.

19 First, we examined the gross change in medial and junctional actin over the period of imaging,
20 roughly st. 13-18 (**Fig. 5A**). Wild-type cells tended to increase both medial and junctional actin
21 localization over time, as expected (**Fig. 5B, C, red violin**). Surprisingly, despite the known role
22 of Shroom3 in the control of actin accumulation (Haigo et al., 2003; Hildebrand, 2005), the
23 majority of *shroom3* crispant cells actually *increased* both junctional and medial actin over the
24 period of imaging (**Fig. 5B, C, blue violin**), though this increase was significantly reduced
25 compared to controls (**Fig. 5B, C**).

26 To explore this surprising result in more detail, we directly compared changes in apical area with
27 changes in actin intensity for each cell. In 838 control cells, we observed that the vast majority
28 displayed a strong reduction in apical area and a strong increase in both junctional and medial
29 actin intensity (**Fig. 5D, E**). As noted in the bulk statistics above, the majority of 147 *shroom3*
30 crispant cells displayed increased actin intensity, but these crispant cells displayed a bimodal
31 distribution of changes in apical area, with some cells constricting and other cells dilating (**Fig.**
32 **5D, E**). Thus, even cells that increase their apical area still also accumulate medial and
33 junctional actin after loss of Shroom3.

34 Finally, for the most granular view, we plotted the correlation between standardized apical area
35 and standardized actin intensity for all cells at all time points (N = ~54k data points). For control
36 cells, apical area displayed a very strong negative correlation with both medial and junctional
37 actin intensity (**Fig. 5F, G**). Notably, however, medial actin was far more strongly correlated to
38 apical area than was junctional actin, consistent with the key function of medial actin described
39 in other systems. Interestingly, despite the relatively modest impact on overall actin
40 accumulation after loss of Shroom3 (**Fig. 5B, C**), the normally strong correlations of apical
41 surface area to medial and junctional actin dynamics were completely abolished in crispant cells
42 (**Fig. 5F, G**). These results demonstrate that while Shroom3 may serve an overall role in actin

1 assembly, this protein's most critical function in neural tube closure *in vivo* is to convert apical
2 actin dynamics into effective apical constriction.

3

4

5

6 **Loss of Shroom3 uncouples actin dynamics from N-cadherin in the anterior neural** 7 **ectoderm.**

8 N-cadherin has been implicated in Shroom3 function and apical constriction in multiple contexts
9 (Lang et al., 2014; Nandadasa et al., 2009; Plageman et al., 2011b), so we next asked how
10 Shroom3 loss impacted N-cadherin dynamics during neural tube closure (**Fig 6A**). In contrast to
11 the surprisingly modest change observed in actin intensity (**Fig. 5B,C**), bulk measurements
12 revealed that *shroom3* crispant cells displayed a profound failure to accumulate medial N-
13 cadherin, and in fact the majority of cells actually reduce N-cadherin levels (**Fig. 6B, blue**
14 **violin**). However, junctional N-cadherin dynamics were more modestly disrupted by Shroom3
15 loss, with many *shroom3* crispant cells showing some degree of junctional N-cadherin
16 accumulation (**Fig. 6C, blue violin**).

17 Next, we performed direct comparisons of changes in apical area to changes in N-cadherin
18 intensity. The vast majority of control cells (81%) reduced their apical area while increasing
19 medial N-cadherin localization (**Fig. 6D, orange**), while *shroom3* crispant cells displayed the
20 converse behavior, with a plurality of cells displaying apical surface dilation over time coupled to
21 a strong *reduction* in medial N-cadherin intensity over time (**Fig. 6D, blue**). Consistent with the
22 bulk statistics above, junctional N-cadherin displayed a distinct phenotype, with cells displaying
23 all possible combinations of apical surface behavior and N-cadherin intensity profiles. (**Fig. 6E**).
24 Finally, correlations of apical area to N-cadherin intensity for all cells at all time-points revealed
25 very strong correlations for both medial and junctional N-cadherin in controls, and these
26 correlations were significantly disrupted by Shroom3 loss (**Fig. 6F, G**).

27 Notably, in all of our analyses, we observed that medial N-cadherin intensity was more strongly
28 affected than was junctional N-cadherin, medial actin or junctional actin, which is intriguing in
29 light of recent reports of key roles for extra-junctional cadherins in actin-dependent processes
30 (Padmanabhan et al., 2017; Sabatini et al., 2011). To further explore this issue, we compared
31 actin and N-cadherin dynamics directly (N = ~54k observations). In control cells, both medial
32 and junctional N-cadherin dynamics display very robust correlation to actin (**Fig. 7**), consistent
33 with our data above. Importantly, however, after Shroom3 loss this correlation was severely
34 disrupted for the medial populations, while the disruptive effect on junctional correlations was far
35 less robust (**Fig. 7**).

36 Together, these results suggest that the primary effect of *shroom3* loss in the anterior neural
37 plate is not on actomyosin contractility *per se*, but rather on the coupling of medial actomyosin
38 contractility with medial N-cadherin accumulation. This result further highlights the possibility of
39 an extra-junctional role for N-cadherin in apical constriction and moreover provides a
40 mechanism to explain our findings above (**Fig. 5D**) that Shroom3 links actin dynamics to
41 changes in apical area.

42

1 **In the posterior neural ectoderm, Shroom3 controls actin and N-cadherin, but not apical**
2 **constriction**

3 As noted above, *shroom3* crispant cells in the posterior neural ectoderm did not display
4 appreciable defects in the change in apical area over the period of our imaging, though cells
5 were overall less constricted than in controls (**Fig. 4C, D**). We reasoned that this result may
6 reflect the complex interplay of Shroom3-mediated apical constriction and PCP-dependent
7 convergent extension cell behaviors (e.g. (McGreevy et al., 2015; Nishimura et al., 2012)). We
8 therefore explored our image data for new insights into the role of Shroom3 in the posterior
9 neural ectoderm.

10 Both junctional and medial actin accumulated over the course of our imaging in control cells in
11 the posterior neural ectoderm, as expected (**Fig. 8A-C, red violins**). In addition, comparisons
12 of changes in area to changes in actin localization revealed that the vast majority of cells
13 decreased their apical area and increased both medial and junctional actin localization (**Fig. 8D,**
14 **E**). Interestingly, however, when comparing the relationship between apical area and actin
15 across all time points in posterior control cells, we found similarly robust correlations for both
16 medial and junctional actin (**Fig. 8F, G**). These correlations are in contrast with our data for the
17 anterior neural ectoderm, where medial actin is more strongly correlated with apical area than
18 junctional actin in control cells (see **Fig. 5F, G**).

19 Examination of actin dynamics in *shroom3* crispant cells revealed clear differences between
20 anterior and posterior neuroepithelial cells. Most strikingly, despite the far less robust apical
21 constriction defect in posterior *shroom3* crispant cells, we observed a much *stronger* defect in
22 accumulation of both medial and junctional actin (compare **Fig. 8B, C** with **Fig. 5B, C**).
23 Moreover, comparing changes in actin to changes in area revealed that many *shroom3* crispant
24 cells undergoing robust apical constriction in the posterior neural plate nonetheless displayed an
25 obvious *loss* of apical actin, suggesting that overall changes in actin localization do not drive
26 apical constriction in posterior *shroom3* crispant cells (**Fig. 8D,E**). In agreement with this idea,
27 both medial and junctional actin localization are relatively poorly correlated with apical area in
28 posterior *shroom3* crispant cells (**Fig. 8F, G**).

29 The dynamics of N-cadherin localization revealed an even more pronounced difference between
30 posterior and anterior (**Fig. 9A**). In control embryos, N-cadherin in the posterior neural
31 ectoderm displayed a far less robust pattern of change over the course of imaging (**Fig. 9B, C,**
32 **red violins**), a clear departure from what was observed anteriorly (Compare to **Fig. 6B, C**). In
33 fact, direct comparisons of overall change in area to overall changes in N-cadherin localization
34 in the posterior revealed two distinct populations of control cells, one in which cells decrease
35 apical area and increased N-cadherin, and another which decreased apical area but also
36 decreased N-cadherin (**Fig. 9D**). A similar pattern was observed for junctional N-cadherin (**Fig.**
37 **9E**). Accordingly, comparisons of apical area to medial or junction N-cadherin across all time
38 points revealed essentially no correlations (**Fig. 9F, G**).

39 Interestingly, *shroom3* crispant cells in the posterior neural plate displayed a fairly uniform
40 behavior, constricting normally, but with nearly all cells also reducing both medial and junctional
41 N-cadherin intensity (**Fig. 9B, C, blue violins, D, E**). Thus, the impact of Shroom3 loss on N-
42 cadherin dynamics is stronger in the posterior than the anterior, even though the effect on apical
43 constriction is far weaker. Together, these results suggest that while a fairly direct relationship
44 between Shroom3, actin, and N-cadherin governs apical constriction anteriorly, the situation is

1 far more complex in the posterior neural ectoderm. One possible explanation for this added
2 complexity is that PCP proteins, such as Vangl2, are known to have a stronger loss-of-function
3 phenotypes in the posterior and likely exert stronger control over cell-cell junction behavior than
4 Shroom3 in posterior neural tube closure; loss of Shroom3 may thus result in aberrant
5 actomyosin localization but relatively unperturbed apical constriction.

6

7 **Cell-cell junction behaviors display distinct differences between the anterior and** 8 **posterior regions of the neural ectoderm**

9 While medial actomyosin appears to be a stronger driver of apical constriction in the anterior
10 neural ectoderm than junctional actomyosin, the primary site of actomyosin activity in the
11 posterior neural ectoderm was unclear. Both actin and N-cadherin accumulation were highly
12 variable at both the medial and junctional domains of posterior cells, and actin and N-cadherin
13 localization were relatively poorly correlated with apical area (**Figs. 8, 9**). To gain additional
14 insights into posterior neural cell behaviors, we used our dataset to quantify the specific
15 behaviors of each individual cell-cell junction in our dataset, incorporating nearly half a million
16 observations from over 10,000 junctions.

17 At the bulk level, junctions in the anterior on average decreased in length, as expected and this
18 trend was severely disrupted in *shroom3* crispant junctions ($p < 2.2 \times 10^{-16}$) (**Fig. 10A**). In the
19 posterior, however, we observed roughly equal growth and shrinkage of control junctions (**Fig.**
20 **10A**). In contrast to anterior *shroom3* junctions, posterior *shroom3* crispant junctions did not
21 show a change in overall junction shrinkage and growth relative to control junctions
22 ($p = 0.2121$) (**Fig 10A**).

23 Junction behaviors during epithelial morphogenesis are frequently polarized with respect to the
24 embryonic axes (Pinheiro and Bellaïche, 2018), so we assigned orientations to all junctions in
25 our dataset. Junctions with a mean orientation less than 45° were designated anteroposterior
26 (AP), as they represent the anterior face of one cell abutting the posterior face of a neighboring
27 cell; junctions with mean orientations greater than 45° were designated as mediolateral
28 (ML) (**Fig. 10B**).

29 In the anterior neural plate, the majority of control junctions displayed robust shrinkage with
30 minor polarization, as evidenced by a difference in distribution of shrinkage and growth between
31 AP and ML junctions (**Fig. 10C**). More specifically, slightly more ML junctions grew than AP
32 junctions, indicating that some degree of tissue elongation or isotropic apical constriction occurs
33 in the anterior neural ectoderm. By contrast, anterior *shroom3* crispant junctions showed no
34 clear bias towards shrinkage or growth in either AP or ML junctions and no polarization of AP
35 versus ML junctions (**Fig. 10C**).

36 While changes in junction length were somewhat polarized in anterior control junctions, neither
37 actin (**Fig. 10E**) or N-cadherin (**Fig. 10G**) dynamics were significantly polarized in those same
38 junctions. Anterior control junctions accumulated both actin and N-cadherin at a similar
39 frequency to which they shrank. Actin and N-cadherin dynamics in anterior *shroom3* crispant
40 junctions were not polarized, similar to control junctions (**Fig. 10E, G**). However, the proportion
41 of junctions that reduced actin and N-cadherin localization decreased in crispant junctions,
42 similar to the increased proportion of crispant junctions that grew over time (**Fig. 10C**). Overall,

1 these results again suggest that Shroom3 may control actomyosin and N-cadherin accumulation
2 at anterior cell-cell junctions.

3 In the posterior neural plate, we observed far more complex patterns of junction behavior. First,
4 junction shrinkage in the posterior neural plate was highly polarized, with AP junctions
5 predominantly shortening and ML junctions predominantly growing (**Fig. 10D**). These patterns
6 of junction behavior are hallmarks of convergent extension and are consistent with previous
7 smaller scale studies of these behaviors in the neural ectoderm (Butler and Wallingford, 2018b;
8 Nishimura et al., 2012; Williams et al., 2014a) and in other tissues (Bertet et al., 2004;
9 Blankenship et al., 2006; Lienkamp et al., 2012). Strikingly, we observed a very similar pattern
10 of behavior in posterior *shroom3* junctions, indicating that Shroom3 has little to no role in
11 polarizing junction behaviors in the posterior neural ectoderm (**Fig. 10D**).

12 However, examination of the patterns of actin and N-cadherin dynamics in the posterior neural
13 ectoderm revealed a more complex phenotype. While we still observed polarization of actin
14 accumulation in AP versus ML control junctions, actin tended to accumulate in both AP and ML
15 junctions (**Fig. 10F**) despite the fact that ML junctions tended to grow (**Fig. 10F**). Strikingly,
16 despite the fact that *shroom3* crispant junctions changed their length in a highly polarized
17 manner (**Fig. 10D**), actin accumulation was depolarized to a significant degree in crispant
18 junctions (**Fig. 10F**), consistent with data from still images in the neural plate of mouse *shroom3*
19 mutants (McGreevy et al., 2015). This defect seems mainly to be due to an increase in actin
20 clearance in *shroom3* AP junctions, despite our observation that *shroom3* AP junctions shrink to
21 a very similar degree as control AP junctions (**Fig. 10D**). These results suggest a disconnect
22 between actin accumulation and junction shrinkage in the posterior neural ectoderm that is
23 amplified upon loss of Shroom3.

24 Even more interesting were the patterns of N-cadherin dynamics. Recall that in cell-level data,
25 we observed nearly equal populations of cells that gained and lost junctional N-cadherin over
26 time (**Fig. 9E**), which we anticipated might reflect junction polarity. What we discovered was
27 that N-cadherin accumulation was again polarized in AP versus ML control junctions, such that
28 shortening AP-oriented junctions were equally likely to accumulate N-cadherin, while ML
29 junctions, which preferentially grow, were far more likely to clear N-cadherin (**Fig. 10H**). Again,
30 *shroom3* junctions presented an unusual phenotype; N-cadherin dynamics were less polarized
31 than length changes in posterior crispant junctions, and the defect again seemed mainly to be
32 an increase in N-cadherin *clearance* at *shroom3* AP junctions (**Fig. 10H**). Thus, posterior
33 *shroom3* crispant junctions display largely normal polarized changes in length (**Fig. 10D**) but
34 show reduced or altered polarity for both actin and N-cadherin dynamics (**Fig. 10F, H**).

35 Together, these results again paint a vivid picture of differences between cell behaviors in the
36 anterior and posterior neural ectoderm. Both control and *shroom3* junctions in the anterior
37 behaved mostly as expected; the majority of both AP and ML control junctions shrank over time,
38 and loss of Shroom3 disrupted junction shrinkage as well as actin and N-cadherin dynamics in a
39 predictable pattern based on whole-cell data. In contrast, shrinkage and growth were highly
40 polarized in the posterior neural ectoderm in both control and *shroom3* crispant junctions,
41 despite polarization of actin and N-cadherin dynamics being reduced in crispant junctions.

42

43

1 Conclusion

2 Understanding the cellular mechanisms contributing to neural tube closure has long challenged
3 embryologists due to the relatively large number of cells involved and the heterogeneity of their
4 behaviors. Indeed, some of the earliest uses of computer simulation in developmental biology
5 focused on understanding the degree to which neural ectoderm cells constrict their apical
6 surfaces during neural tube closure (Jacobson and Gordon, 1976). Since then, our
7 understanding of the genetics and cellular mechanisms of neural tube closure has broadly
8 improved. Hundreds of mutations affecting neural tube closure have been identified (Harris and
9 Juriloff, 2010), and interactions between neural tube closure genes are becoming better
10 understood (McGreevy et al., 2015; Murdoch et al., 2014). However, while time lapse imaging of
11 single cell behaviors in chicks, frogs, and mice have provides several key insights (Butler and
12 Wallingford, 2018a; Christodoulou and Skourides, 2015; Davidson and Keller, 1999; Galea et
13 al., 2017; Massarwa and Niswander, 2013; Molè et al., 2020; Ossipova et al., 2015; Pyrgaki et
14 al., 2010; Wallingford and Harland, 2002; Williams et al., 2014b), our understanding of the cell
15 biology of neural tube closure still lags substantial behind our understanding of the genetics.

16 Recent research has begun to bridge the gap between the breadth of our genetic resources and
17 the scale of neural tube closure as a process; *in toto* imaging has captured neural tube closure
18 as one facet of overall mouse development (McDole et al., 2018), tissue-scale imaging of has
19 revealed the cell biological basis of ciliopathy-related NTDs (Brooks et al., 2020). In a
20 complement to these advancements, we have used high-resolution, but tissue-scale, time-lapse
21 imaging of both actin and N-cadherin followed by cell-tracking analysis to gain several new
22 mechanistic insights into the process of apical constriction during neural tube closure.

23 First, we show that anterior and posterior neural ectoderm cells undergo apical constriction to
24 differing degrees and by different constrictive mechanisms. Further, we show that mosaic
25 mutation of *shroom3* similarly results in different phenotypes in the anterior and posterior. This
26 is consistent with how disruption of *shroom3* has been shown to have stronger effects on
27 anterior neural tube closure (Hildebrand 1999, Haigo 2003, McGreevy 2015). Conversely,
28 disruption of PCP signaling has been shown to have stronger defects in posterior neural tube
29 closure (e.g. (Galea et al., 2018; Murdoch et al., 2014)). Applying the approach described here
30 to analysis of PCP protein localization should be highly illuminating.

31 Second, we show that changes in apical area in the anterior neural ectoderm are more strongly
32 correlated with changes in medial actomyosin localization versus junctional actomyosin,
33 indicating that contractility driving apical constriction is more likely to be generated at the medial
34 cell surface. Our results on medial actin localization are largely consistent with smaller scale
35 studies in both *Xenopus* and mice (Christodolou 2015, Suzuki 2017, Brown 2018) and moreover
36 reflect mechanisms described in more detail in the context of *Drosophila* and *C. elegans*
37 gastrulation (Martin et al., 2009; Roh-Johnson et al., 2012). Conversely, our data shows that
38 both medial and junctional actin localization have similar correlations with apical area in the
39 posterior neural ectoderm, suggesting actomyosin contractility may be more balanced across
40 these medial and junctional domains in this region.

41 Third, we show that N-cadherin accumulates at the medial surfaces of constricting cells in the
42 anterior neural ectoderm, but that N-cadherin localization poorly correlates with apical
43 constriction in the posterior. Interestingly, our mechanistic analysis suggests that anterior
44 *shroom3* crispant cells fail to constrict less from a lack of actomyosin accumulation and more

1 from an inability to accumulate N-cadherin at the medial surface of cells. This is consistent with
2 a previously reported genetic interaction between *shroom3* and *N-cadherin* (Plageman et al.,
3 2011b), and suggests that a Shroom3-N-cadherin pathway may drive anterior apical constriction
4 during neural tube closure.

5 The study of developmental biology in the 21st century is marked by explosive increases in the
6 size of experiments – advancements in proteomics and transcriptomics are providing an
7 unprecedented depth to our understanding of the molecular workings of cells in embryos. Thus,
8 it is of special importance that we use advances in imaging and data analysis to ask what those
9 cells *actually do and how they do it*. The work here is therefore significant for providing
10 quantitative insights into the interplay of gene function, protein localization and cell behavior
11 during a biomedically important process in vertebrate embryogenesis.

12

13 **Acknowledgments**

14 Special thanks to Pavak Shah and Claire McWhite for assistance with coding and data analysis
15 and to the Wallingford lab for manuscript comments. This work was funded by NICHD Ruth L.
16 Kirschstein NRSA F32 HD094521 for AB and R01HD099191 to JW.

17

18

19 **Materials and Methods**

20 Animals

21 Wild-type *Xenopus tropicalis* frogs were obtained from the National Xenopus Resource, Woods
22 Hole, MA (Horb et al., 2019).

23 Injections

24 Wild-type *X. tropicalis* eggs were fertilized *in vitro* using sperm from wild-type *X. tropicalis* males
25 using standard methods.

26 *X. tropicalis* embryos were moved to 1/9x MMR + 2% Ficoll, then injected in both dorsal
27 blastomeres at the 4-cell stage with 50pg LifeAct-RFP mRNA and 150pg *Xenopus* N-cadherin-
28 GFP mRNA. In CRISPR-injected embryos, at the 8-cell stage, one dorsal blastomere was
29 injected with 1ng Cas9 protein (PNA Bio), 250pg *shroom3*-targeted sgRNA
30 (Synthego)(**Methods Appendix Fig. 1A**), and 60pg membrane(CAAX)-BFP mRNA.

31 CRISPR genotyping

32 To test the efficacy of our CRISPR injections *in vivo*, we injected wild-type *X. tropicalis* with the
33 above-described Cas9+sgRNA combination in the following cells and stages: 2x injections into
34 1-cell stage embryos, 1x injections into each blastomere of 2-cell stage embryos, 1x injections
35 into 2 blastomeres of the 4-cell stage embryo, and 1x injections into all blastomeres of 4-cell
36 stage embryos (**Methods Appendix Fig. 1B**). Uninjected embryos that did not receive any
37 Cas9+sgRNA were used as controls.

1 Embryos were allowed to grow to approximately Nieuwkoop and Faber (NF) stage 40 and then
2 were subjected to whole-embryo DNA extraction. PCR products spanning the *shroom3* target
3 site were generated from each embryo and separated by capillary electrophoresis for fragment
4 analysis. Fragment analysis data was analyzed in R using the *Fragman* package (Covarrubias-
5 Pazaran et al., 2016).

6 Uninjected embryos did not have any indel products at the *shroom3* locus and thus produced
7 one sharp peak at 431 base pairs, corresponding to the size of the wild-type *shroom3* PCR
8 product (**Methods Appendix Fig. 1B**). By contrast, CRISPR-injected embryos returned little to
9 no PCR products at this size (**Methods Appendix Fig. 1B**, dashed red line), indicating that the
10 *shroom3* target site was being efficiently cut by Cas9 and repaired by error-prone pathways.
11 The exception to this were the embryos of which only 2 blastomeres at the 4-cell stage were
12 injected with Cas9+sgRNA; as expected, fragments of the wild-type size were detected that
13 theoretically correspond to the uninjected blastomere lineages (**Methods Appendix Fig. 1B**).
14 Overall, these results indicate that our Cas9+sgRNA combination efficiently cleaves the
15 *shroom3* target site *in vivo*.

16 Imaging

17 Injected embryos were held at 25C until they reached NF stage 12.5. At NF stage 12.5, vitelline
18 envelopes were removed from embryos and embryos were allowed to “relax” for 30 minutes.
19 Embryos were then mounted in imaging chambers and positioned for imaging of either the
20 anterior or posterior neural plate.

21 Embryos were imaged on a Nikon A1R confocal microscope using the resonant scanner mode.
22 Image quality, Z-stacking, and XY tiling were balanced to generate optimal 3D images of the
23 neural plate at a rate of 1 frame per minute. Ultimately, movies of 7 embryos were of sufficient
24 length and quality for analysis. Tissue geometry and *shroom3* crispant calling of the initial frame
25 of each of these embryos is presented in **Methods Appendix Fig. 2**.

26 Image Analysis

27 Raw 3D images were projected to 2D via maximum intensity and underwent initial segmentation
28 of cell boundaries using the FIJI plugin Tissue Analyzer (Aigouy et al., 2010; Aigouy et al.,
29 2016). The segmentation of an initial frame was hand-corrected, and this hand-corrected
30 segmentation was used to train a classifier using the program CSML (Ota et al., 2018). CSML
31 was used to generate segmentation for subsequent frames, which were then further hand-
32 corrected in Tissue Analyzer.

33 After hand-correction, Tissue Analyzer was used to track both cell surfaces and cell junctions,
34 then generate a database of measurements of size and fluorescent intensities for each cell and
35 junction over time. Values for medial and junctional localization of imaged markers in cells were
36 calculated as average pixel fluorescence intensity across the entirety of each respective
37 domain. Similarly, localization of imaged markers to individual junctions was calculated as an
38 average across the entire junction.

39 For individual junctions, errors in junction length caused by Z-displacement and projection were
40 corrected in Matlab (code courtesy of Pavak Shah).

41 Tissue Analyzer databases were imported to R and further analyzed and manipulated primarily
42 using the *tidyverse* package (R Core Team, 2020; Wickham et al., 2019).

1 Data Analysis

2 Cell tracks shorter than 30 frames and junction tracks shorter than 15 frames were discarded.

3 Embryo “b” had a fluorescence anomaly during imaging that resulted in a reduction in overall
4 fluorescence followed by a recovery (**Methods Appendix Fig. 3A,B**). Cells were tracked
5 through the anomaly (**Methods Appendix Fig. 3C**), but fluorescent values for the frames 23 to
6 45 were discarded (**Methods Appendix Fig. 3**, red dashed box).

7 Cells were determined to be control versus *shroom3* crispant by a membrane-BFP localization
8 threshold specific to each embryo (**Fig. 4B**, middle panel). Crispant calls were then manually
9 annotated in cases along the mosaic interface where thresholding produced crispant calls
10 deemed incorrect.

11 Individual junctions were determined to be control versus *shroom3* crispant versus mosaic
12 interface based on the status of the cells the junction was situated between. Control junctions
13 are situated between two control cells, *shroom3* crispant junctions are situated between two
14 *shroom3* crispant cells, and mosaic interface junctions are situated between a control and a
15 *shroom3* crispant cell (**Fig. 4B**, lower panel). In this study, we excluded cells and junctions at
16 the mosaic interface from our analysis.

17 Junction orientations were corrected so that the mediolateral axis of the embryo was set at 0°
18 and the anteroposterior axis of the embryo was set at 90° (**Figure 10A**).

19 Individual cell and junction tracks were smoothed by averaging over a 7 frame/minute window
20 (**Methods Appendix Fig. 4B**). Individual cell tracks were further mean-centered and
21 standardized so that variables are measured in standard deviations rather than fluorescence or
22 size units (**Methods Appendix Fig. 4C**). This standardization allows us to analyze dynamics of
23 cell size and protein localization across a population of cells while controlling for initial size and
24 fluorescence of cells. In an example embryo, cells begin and end tracking with a variety of
25 apical surface areas (**Methods Appendix Fig. 4D'**), but once the cell tracks are mean-centered
26 and standardized it becomes clear that the cells are behaving similarly at a population level
27 (**Methods Appendix Fig. 4C''**).

28 1D statistical comparisons were performed using the Kolmogorov-Smirnov (K-S) test via the R
29 *ks.test* function (R Core Team, 2020). 2D statistical comparisons were performed using the
30 Peacock Test, a 2D implementation of the K-S test (Fasano and Franceschini, 1987; Peacock,
31 1983). Peacock tests were performed using the R *Peacock.test* package (Xiao, 2016; Xiao,
32 2017).

33

34

35

36

37

38

39

1

2 **References:**

3

- 4 Aigouy, B., R. Farhadifar, D.B. Staple, A. Sagner, J.C. Roper, F. Julicher, and S. Eaton. 2010. Cell flow
5 reorients the axis of planar polarity in the wing epithelium of *Drosophila*. *Cell*. 142:773-786.
- 6 Aigouy, B., D. Umetsu, and S. Eaton. 2016. Segmentation and Quantitative Analysis of Epithelial Tissues.
7 *Methods Mol Biol*. 1478:227-239.
- 8 Aslan, Y., E. Tadjuidje, A.M. Zorn, and S.W. Cha. 2017. High-efficiency non-mosaic CRISPR-mediated
9 knock-in and indel mutation in F0 *Xenopus*. *Development*. 144:2852-2858.
- 10 Bertet, C., L. Sulak, and T. Lecuit. 2004. Myosin-dependent junction remodelling controls planar cell
11 intercalation and axis elongation. *Nature*. 429:667-671.
- 12 Blankenship, J.T., S.T. Backovic, J.S. Sanny, O. Weitz, and J.A. Zallen. 2006. Multicellular rosette
13 formation links planar cell polarity to tissue morphogenesis. *Dev Cell*. 11:459-470.
- 14 Brooks, E.R., M.T. Islam, K.V. Anderson, and J.A. Zallen. 2020. Sonic hedgehog signaling directs patterned
15 cell remodeling during cranial neural tube closure. *Elife*. 9.
- 16 Brown, J.M., and M.J. García-García. 2018. Secretory pathway calcium ATPase 1 (SPCA1) controls mouse
17 neural tube closure by regulating cytoskeletal dynamics. *Development*. 145.
- 18 Butler, M.T., and J.B. Wallingford. 2018a. Spatial and temporal analysis of PCP protein dynamics during
19 neural tube closure. *Elife*. 7.
- 20 Butler, M.T., and J.B. Wallingford. 2018b. Spatial and temporal analysis of PCP protein dynamics during
21 neural tube closure. *Elife (Cambridge)*. 7:e36456.
- 22 Christodoulou, N., and P.A. Skourides. 2015. Cell-Autonomous Ca(2+) Flashes Elicit Pulsed Contractions
23 of an Apical Actin Network to Drive Apical Constriction during Neural Tube Closure. *Cell Rep*.
24 13:2189-2202.
- 25 Coravos, J.S., and A.C. Martin. 2016. Apical Sarcomere-like Actomyosin Contracts Nonmuscle *Drosophila*
26 Epithelial Cells. *Dev Cell*. 39:346-358.
- 27 Covarrubias-Pazaran, G., L. Diaz-Garcia, B. Schlautman, W. Salazar, and J. Zalapa. 2016. Fragman: an R
28 package for fragment analysis. *BMC Genetics*. 17:62.
- 29 Das, D., J.K. Zalewski, S. Mohan, T.F. Plegeman, A.P. VanDemark, and J.D. Hildebrand. 2014. The
30 interaction between Shroom3 and Rho-kinase is required for neural tube morphogenesis in
31 mice. *Biology Open*. 3:850-860.
- 32 Davidson, L.A., and R.E. Keller. 1999. Neural tube closure in *Xenopus laevis* involves medial migration,
33 directed protrusive activity, cell intercalation and convergent extension. *Development*.
34 126:4547-4556.
- 35 Deshwar, A.R., N. Martin, P. Shannon, and D. Chitayat. 2020. A homozygous pathogenic variant in
36 SHROOM3 associated with anencephaly and cleft lip and palate. *Clinical Genetics*. n/a.
- 37 Durbin, M.D., J. O'Kane, S. Lorentz, A.B. Firulli, and S.M. Ware. 2020. SHROOM3 is downstream of the
38 planar cell polarity pathway and loss-of-function results in congenital heart defects. *Dev Biol*.
39 464:124-136.
- 40 Fasano, G., and A. Franceschini. 1987. A multidimensional version of the Kolmogorov–Smirnov test.
41 *Monthly Notices of the Royal Astronomical Society*. 225:155-170.
- 42 Galea, G.L., Y.-J. Cho, G. Galea, M.A. Molè, A. Rolo, D. Savery, D. Moulding, L.H. Culshaw, E.
43 Nikolopoulou, N.D.E. Greene, and A.J. Copp. 2017. Biomechanical coupling facilitates spinal
44 neural tube closure in mouse embryos. *Proceedings of the National Academy of Sciences*.

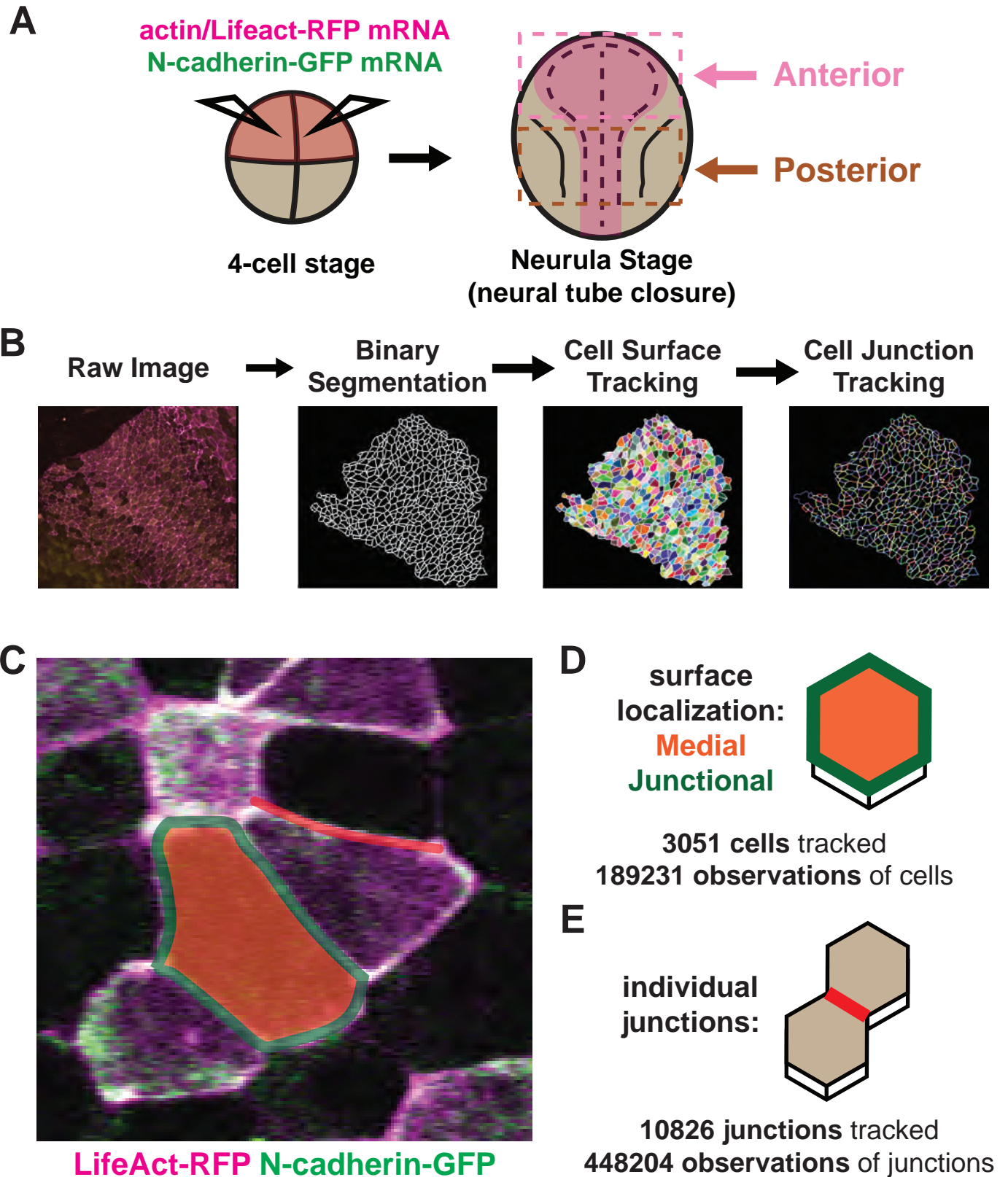
- 1 Galea, G.L., O. Nychyk, M.A. Mole, D. Moulding, D. Savery, E. Nikolopoulou, D.J. Henderson, N.D.E.
2 Greene, and A.J. Copp. 2018. Vangl2 disruption alters the biomechanics of late spinal
3 neurulation leading to spina bifida in mouse embryos. *Dis Model Mech.* 11.
- 4 Haigo, S.L., J.D. Hildebrand, R.M. Harland, and J.B. Wallingford. 2003. Shroom induces apical constriction
5 and is required for hinge point formation during neural tube closure. *Curr Biol.* 13:2125-2137.
- 6 Harris, M.J., and D.M. Juriloff. 2010. An update to the list of mouse mutants with neural tube closure
7 defects and advances toward a complete genetic perspective of neural tube closure. *Birth*
8 *Defects Res A Clin Mol Teratol.* 88:653-669.
- 9 Hildebrand, J.D. 2005. Shroom regulates epithelial cell shape via the apical positioning of an actomyosin
10 network. *J Cell Sci.* 118:5191-5203.
- 11 Hildebrand, J.D., and P. Soriano. 1999. Shroom, a PDZ domain-containing actin-binding protein, is
12 required for neural tube morphogenesis in mice. *Cell.* 99:485-497.
- 13 Horb, M., M. Wlizla, A. Abu-Daya, S. McNamara, D. Gajdasik, T. Igawa, A. Suzuki, H. Ogino, A. Noble, J.
14 Robert, C. James-Zorn, and M. Guille. 2019. Xenopus Resources: Transgenic, Inbred and Mutant
15 Animals, Training Opportunities, and Web-Based Support. *Front Physiol.* 10:387.
- 16 Ichikawa, T., C. Stuckenholtz, and L.A. Davidson. 2020. Non-junctional role of Cadherin3 in cell migration
17 and contact inhibition of locomotion via domain-dependent, opposing regulation of Rac1. *Sci*
18 *Rep.* 10:17326.
- 19 Jacobson, A.G., and R. Gordon. 1976. Changes in the shape of the developing vertebrate nervous system
20 analyzed experimentally, mathematically and by computer simulation. *J Exp Zool.* 197:191-246.
- 21 Kakebeen, A.D., A.D. Chitsazan, M.C. Williams, L.M. Saunders, and A.E. Wills. 2020. Chromatin
22 accessibility dynamics and single cell RNA-Seq reveal new regulators of regeneration in neural
23 progenitors. *Elife.* 9.
- 24 Kibar, Z., K.J. Vogan, N. Groulx, M.J. Justice, D.A. Underhill, and P. Gros. 2001. Ltap, a mammalian
25 homolog of Drosophila Strabismus/Van Gogh, is altered in the mouse neural tube mutant Loop-
26 tail. *Nat Genet.* 28:251-255.
- 27 Kroll, F., G.T. Powell, M. Ghosh, G. Gestri, P. Antinucci, T.J. Hearn, H. Tunbak, S. Lim, H.W. Dennis, J.M.
28 Fernandez, D. Whitmore, E. Dreosti, S.W. Wilson, E.J. Hoffman, and J. Rihel. 2021. A simple and
29 effective F0 knockout method for rapid screening of behaviour and other complex phenotypes.
30 *Elife.* 10.
- 31 Lang, R.A., K. Herman, A.B. Reynolds, J.D. Hildebrand, and T.F. Plageman. 2014. p120-catenin-dependent
32 junctional recruitment of Shroom3 is required for apical constriction during lens pit
33 morphogenesis. *Development.* 141:3177.
- 34 Lee, C., H.M. Scherr, and J.B. Wallingford. 2007. Shroom family proteins regulate gamma-tubulin
35 distribution and microtubule architecture during epithelial cell shape change. *Development.*
36 134:1431-1441.
- 37 Lemay, P., M.C. Guyot, E. Tremblay, A. Dionne-Laporte, D. Spiegelman, E. Henrion, O. Diallo, P. De
38 Marco, E. Merello, C. Massicotte, V. Desilets, J.L. Michaud, G.A. Rouleau, V. Capra, and Z. Kibar.
39 2015. Loss-of-function de novo mutations play an important role in severe human neural tube
40 defects. *J Med Genet.* 52:493-497.
- 41 Lienkamp, S.S., K. Liu, C.M. Karner, T.J. Carroll, O. Ronneberger, J.B. Wallingford, and G. Walz. 2012.
42 Vertebrate kidney tubules elongate using a planar cell polarity-dependent, rosette-based
43 mechanism of convergent extension. *Nat Genet.* 44:1382-1387.
- 44 Martin, A.C., and B. Goldstein. 2014. Apical constriction: themes and variations on a cellular mechanism
45 driving morphogenesis. *Development.* 141:1987-1998.
- 46 Martin, A.C., M. Kaschube, and E.F. Wieschaus. 2009. Pulsed contractions of an actin-myosin network
47 drive apical constriction. *Nature.* 457:495-499.

- 1 Massarwa, R., and L. Niswander. 2013. In toto live imaging of mouse morphogenesis and new insights
2 into neural tube closure. *Development*. 140:226-236.
- 3 McDole, K., L. Guignard, F. Amat, A. Berger, G. Malandain, L.A. Royer, S.C. Turaga, K. Branson, and P.J.
4 Keller. 2018. In Toto Imaging and Reconstruction of Post-Implantation Mouse Development at
5 the Single-Cell Level. *Cell*. 175:859-876.e833.
- 6 McGreevy, E.M., D. Vijayraghavan, L.A. Davidson, and J.D. Hildebrand. 2015. Shroom3 functions
7 downstream of planar cell polarity to regulate myosin II distribution and cellular organization
8 during neural tube closure. *Biol Open*. 4:186-196.
- 9 Molè, M.A., G.L. Galea, A. Rolo, A. Weberling, O. Nychyk, S.C. De Castro, D. Savery, R. Fässler, P. Ybot-
10 González, N.D.E. Greene, and A.J. Copp. 2020. Integrin-Mediated Focal Anchorage Drives
11 Epithelial Zippering during Mouse Neural Tube Closure. *Dev Cell*. 52:321-334.e326.
- 12 Morita, H., S. Nandadasa, T.S. Yamamoto, C. Terasaka-Iioka, C. Wylie, and N. Ueno. 2010. Nectin-2 and
13 N-cadherin interact through extracellular domains and induce apical accumulation of F-actin in
14 apical constriction of *Xenopus* neural tube morphogenesis. *Development*. 137:1315-1325.
- 15 Murdoch, J.N., C. Damrau, A. Paudyal, D. Bogani, S. Wells, N.D. Greene, P. Stanier, and A.J. Copp. 2014.
16 Genetic interactions between planar cell polarity genes cause diverse neural tube defects in
17 mice. *Dis Model Mech*. 7:1153-1163.
- 18 Murphy, S.L., J. Xu, K.D. Kochanek, and E. Arias. 2018. Mortality in the United States, 2017. *NCHS data*
19 *brief*:1-8.
- 20 Nandadasa, S., Q. Tao, N.R. Menon, J. Heasman, and C. Wylie. 2009. N- and E-cadherins in *Xenopus* are
21 specifically required in the neural and non-neural ectoderm, respectively, for F-actin assembly
22 and morphogenetic movements. *Development*. 136:1327-1338.
- 23 Nieuwkoop, P.D., and J. Faber. 1994. Normal table of *Xenopus laevis* (Daudin): A systematical and
24 chronological survey of the development from the fertilized egg till the end of metamorphosis.
25 Garland Pub, New York.
- 26 Nikolopoulou, E., G.L. Galea, A. Rolo, N.D. Greene, and A.J. Copp. 2017. Neural tube closure: cellular,
27 molecular and biomechanical mechanisms. *Development*. 144:552-566.
- 28 Nishimura, T., H. Honda, and M. Takeichi. 2012. Planar cell polarity links axes of spatial dynamics in
29 neural-tube closure. *Cell*. 149:1084-1097.
- 30 Nishimura, T., and M. Takeichi. 2008. Shroom3-mediated recruitment of Rho kinases to the apical cell
31 junctions regulates epithelial and neuroepithelial planar remodeling. *Development*. 135:1493-
32 1502.
- 33 Ossipova, O., I. Chuykin, C.W. Chu, and S.Y. Sokol. 2015. Vangl2 cooperates with Rab11 and Myosin V to
34 regulate apical constriction during vertebrate gastrulation. *Development*. 142:99-107.
- 35 Ota, R., T. Ide, and T. Michiue. 2018. A novel cell segmentation method for developing embryos using
36 machine learning. *bioRxiv*:288720.
- 37 Padmanabhan, A., H.T. Ong, and R. Zaidel-Bar. 2017. Non-junctional E-Cadherin Clusters Regulate the
38 Actomyosin Cortex in the *C. elegans* Zygote. *Curr Biol*. 27:103-112.
- 39 Peacock, J.A. 1983. Two-dimensional goodness-of-fit testing in astronomy. *Monthly Notices of the Royal*
40 *Astronomical Society*. 202:615-627.
- 41 Pinheiro, D., and Y. Bellaïche. 2018. Mechanical Force-Driven Adherens Junction Remodeling and
42 Epithelial Dynamics. *Dev Cell*. 47:3-19.
- 43 Plageman, T.F., Jr., B.K. Chauhan, C. Yang, F. Jaudon, X. Shang, Y. Zheng, M. Lou, A. Debant, J.D.
44 Hildebrand, and R.A. Lang. 2011a. A Trio-RhoA-Shroom3 pathway is required for apical
45 constriction and epithelial invagination. *Development*. 138:5177-5188.
- 46 Plageman, T.F., Jr., M.I. Chung, M. Lou, A.N. Smith, J.D. Hildebrand, J.B. Wallingford, and R.A. Lang. 2010.
47 Pax6-dependent Shroom3 expression regulates apical constriction during lens placode
48 invagination. *Development*. 137:405-415.

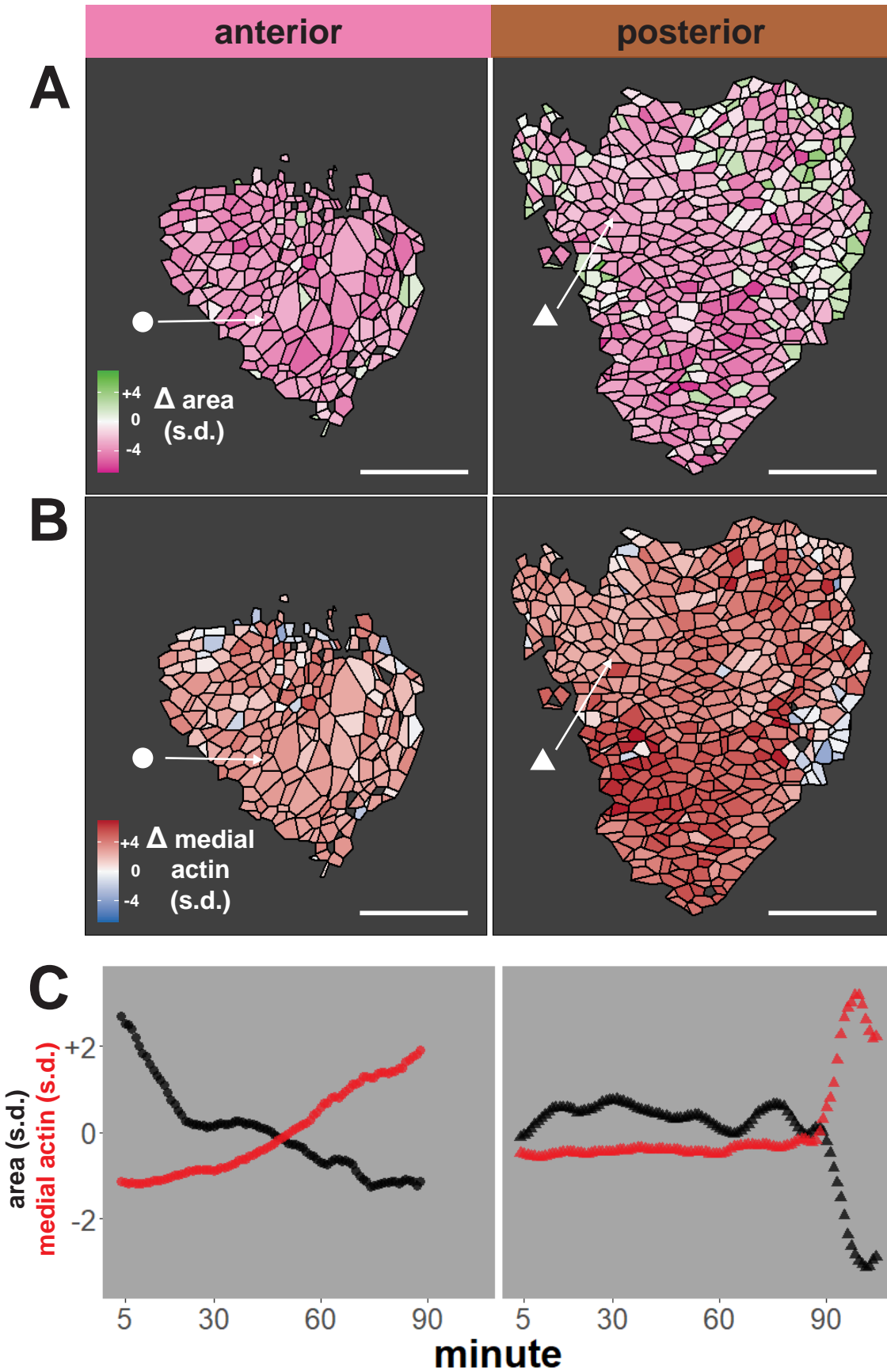
- 1 Plageman, T.F., Jr., A.L. Zacharias, P.J. Gage, and R.A. Lang. 2011b. Shroom3 and a Pitx2-N-cadherin
2 pathway function cooperatively to generate asymmetric cell shape changes during gut
3 morphogenesis. *Dev Biol.* 357:227-234.
- 4 Pyrgaki, C., P. Trainor, A.K. Hadjantonakis, and L. Niswander. 2010. Dynamic imaging of mammalian
5 neural tube closure. *Dev Biol.* 344:941-947.
- 6 R Core Team. 2020. R: A Language and Environment for Statistical Computing. R Foundation for
7 Statistical Computing, Vienna, Austria.
- 8 Rebman, J.K., K.E. Kirchoff, and G.S. Walsh. 2016. Cadherin-2 Is Required Cell Autonomously for
9 Collective Migration of Facial Branchiomotor Neurons. *PLoS ONE.* 11:e0164433.
- 10 Riedl, J., A.H. Crevenna, K. Kessenbrock, J.H. Yu, D. Neukirchen, M. Bista, F. Bradke, D. Jenne, T.A. Holak,
11 Z. Werb, M. Sixt, and R. Wedlich-Soldner. 2008. Lifeact: a versatile marker to visualize F-actin.
12 *Nat Methods.* 5:605-607.
- 13 Roh-Johnson, M., G. Shemer, C.D. Higgins, J.H. McClellan, A.D. Werts, U.S. Tulu, L. Gao, E. Betzig, D.P.
14 Kiehart, and B. Goldstein. 2012. Triggering a cell shape change by exploiting preexisting
15 actomyosin contractions. *Science.* 335:1232-1235.
- 16 Sabatini, P.J., M. Zhang, R.V. Silverman-Gavrila, and M.P. Bendeck. 2011. Cadherins at cell-autonomous
17 membrane contacts control macropinocytosis. *J Cell Sci.* 124:2013-2020.
- 18 Sako, Y., A. Nagafuchi, S. Tsukita, M. Takeichi, and A. Kusumi. 1998. Cytoplasmic regulation of the
19 movement of E-cadherin on the free cell surface as studied by optical tweezers and single
20 particle tracking: corralling and tethering by the membrane skeleton. *J Cell Biol.* 140:1227-1240.
- 21 Schindelin, J., I. Arganda-Carreras, E. Frise, V. Kaynig, M. Longair, T. Pietzsch, S. Preibisch, C. Rueden, S.
22 Saalfeld, B. Schmid, J.Y. Tinevez, D.J. White, V. Hartenstein, K. Eliceiri, P. Tomancak, and A.
23 Cardona. 2012. Fiji: an open-source platform for biological-image analysis. *Nat Methods.* 9:676-
24 682.
- 25 Simões Sde, M., A. Mainieri, and J.A. Zallen. 2014. Rho GTPase and Shroom direct planar polarized
26 actomyosin contractility during convergent extension. *J Cell Biol.* 204:575-589.
- 27 Suzuki, M., M. Sato, H. Koyama, Y. Hara, K. Hayashi, N. Yasue, H. Imamura, T. Fujimori, T. Nagai, R.E.
28 Campbell, and N. Ueno. 2017. Distinct intracellular Ca²⁺ dynamics regulate apical constriction
29 and differentially contribute to neural tube closure. *Development.* 144:1307-1316.
- 30 Szenker-Ravi, E., U. Altunoglu, M. Leushacke, C. Bosso-Lefèvre, M. Khatoo, H. Thi Tran, T. Naert, R.
31 Noelanders, A. Hajamohideen, C. Beneteau, S.B. de Sousa, B. Karaman, X. Latypova, S. Başaran,
32 E.B. Yücel, T.T. Tan, L. Vlaminck, S.S. Nayak, A. Shukla, K.M. Girisha, C. Le Caignec, N. Soshnikova,
33 Z.O. Uyguner, K. Vleminckx, N. Barker, H. Kayserili, and B. Reversade. 2018. RSPO2 inhibition of
34 RNF43 and ZNRF3 governs limb development independently of LGR4/5/6. *Nature.* 557:564-569.
- 35 Wallingford, J.B., and R.M. Harland. 2002. Neural tube closure requires Dishevelled-dependent
36 convergent extension of the midline. *Development.* 129:5815-5825.
- 37 Wallingford, J.B., L.A. Niswander, G.M. Shaw, and R.H. Finnell. 2013. The continuing challenge of
38 understanding, preventing, and treating neural tube defects. *Science.* 339:1222002.
- 39 Wang, J., N.S. Hamblet, S. Mark, M.E. Dickinson, B.C. Brinkman, N. Segil, S.E. Fraser, P. Chen, J.B.
40 Wallingford, and A. Wynshaw-Boris. 2006. Dishevelled genes mediate a conserved mammalian
41 PCP pathway to regulate convergent extension during neurulation. *Development.* 133:1767-
42 1778.
- 43 Wickham, H., M. Averick, J. Bryan, W. Chang, L. D'Agostino McGowan, R. François, G. Grolemond, A.
44 Hayes, L. Henry, J. Hester, M. Kuhn, T.L. Pedersen, E. Miller, S.M. Bache, K. Müller, D. Robinson,
45 D.P. Seidel, V. Spinu, K. Takahashi, D. Vaughan, C. Wilke, K. Woo, and H. Yutani. 2019. Welcome
46 to the Tidyverse. *Journal of Open Source Software.*
- 47 Williams, M., W. Yen, X. Lu, and A. Sutherland. 2014a. Distinct apical and basolateral mechanisms drive
48 PCP-dependent convergent extension of the mouse neural plate. *Dev. Cell.* 29:34-46.

- 1 Williams, M., W. Yen, X. Lu, and A. Sutherland. 2014b. Distinct apical and basolateral mechanisms drive
2 planar cell polarity-dependent convergent extension of the mouse neural plate. *Dev Cell*. 29:34-
3 46.
- 4 Willsey, H.R., Y. Xu, A. Everitt, J. Dea, C.R.T. Exner, A.J. Willsey, M.W. State, and R.M. Harland. 2020. The
5 neurodevelopmental disorder risk gene DYRK1A is required for ciliogenesis and control of brain
6 size in *Xenopus* embryos. *Development*. 147.
- 7 Wu, Y., P. Kanchanawong, and R. Zaidel-Bar. 2015. Actin-delimited adhesion-independent clustering of
8 E-cadherin forms the nanoscale building blocks of adherens junctions. *Dev Cell*. 32:139-154.
- 9 Xiao, Y. 2016. Peacock.test: Two and Three Dimensional Kolmogorov-Smirnov Two-Sample Tests.
- 10 Xiao, Y. 2017. A fast algorithm for two-dimensional Kolmogorov–Smirnov two sample tests.
11 *Computational Statistics & Data Analysis*. 105:53-58.

12



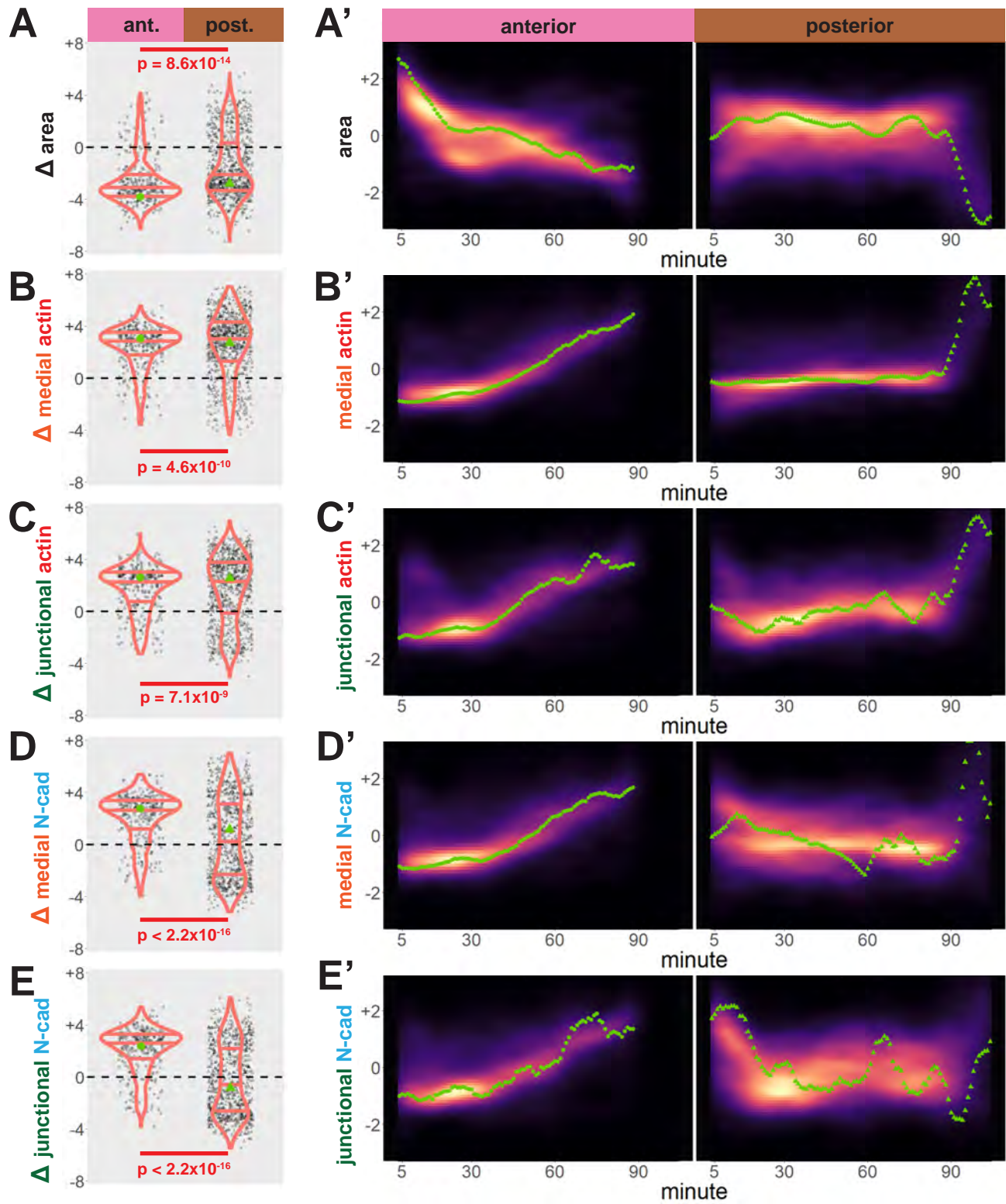
1 **Figure 1: Tissue-level imaging and analysis of contractile protein dynamics during neural**
2 **tube closure in *Xenopus*.** **A.** Schematic of mRNA injections and subsequent imaged regions of
3 the *Xenopus tropicalis* embryo. **B.** Cell segmentation and tracking workflow. Binary
4 Segmentation, Cell Surface Tracking, and Cell Junction Tracking were all generated using
5 Tissue Analyzer. **C.** Example *Xenopus* cells with analyzed subcellular domains labeled. Orange
6 label = medial, green label = junctional, red label = individual junction. **D.** Schematic and N
7 values of whole cell measurements. **E.** Schematic and N values of individual cell junction
8 measurements.
9



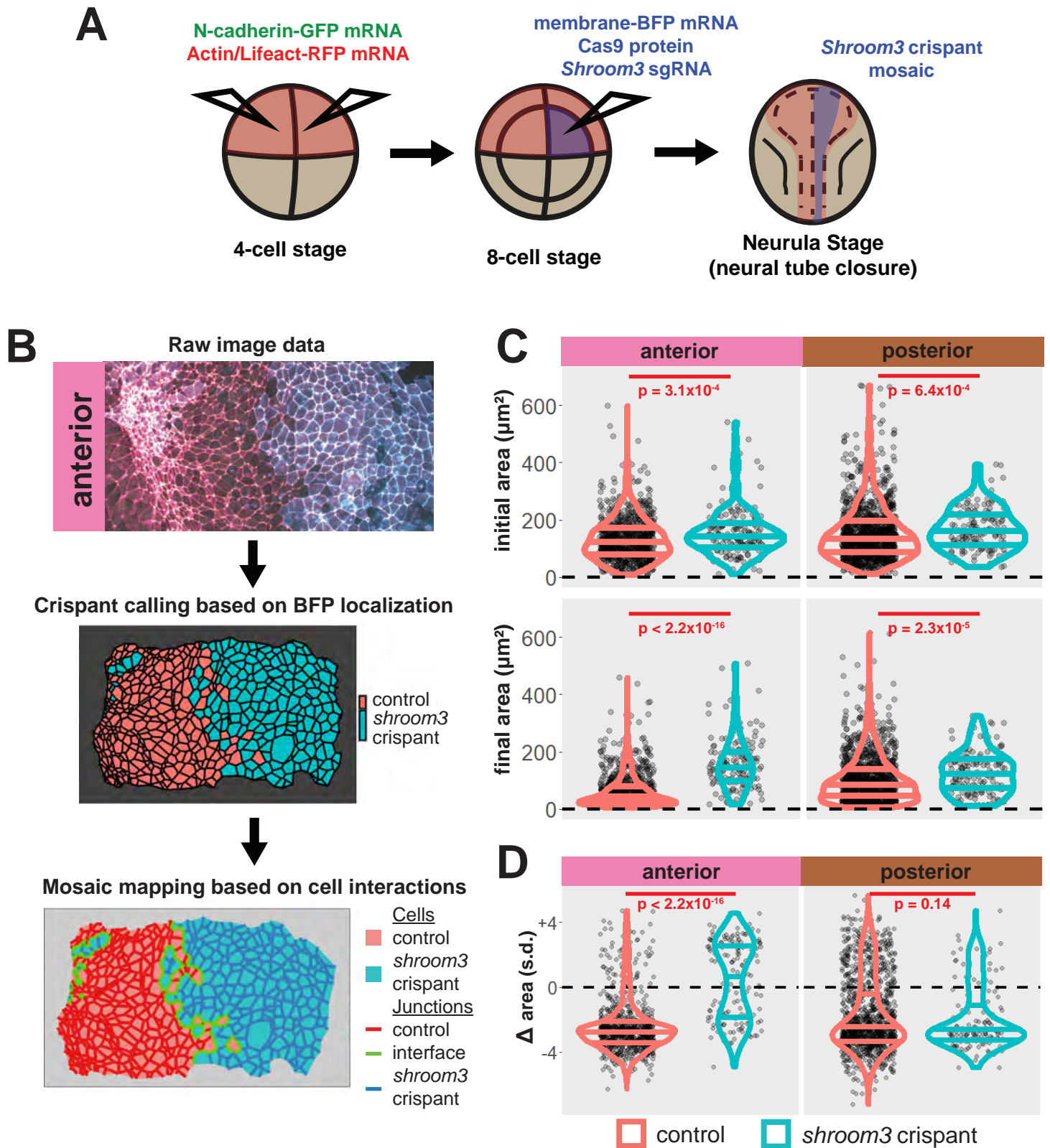
Baldwin et al. Figure 2

1 **Figure 2: Tissue-level analysis of individual cell behaviors reveals dynamic**
2 **heterogeneity. A.** Overall change (Δ) in apical surface area (standardized) across anterior (left)
3 and posterior (right) control embryos. **B.** Overall change in medial LifeAct/actin localization
4 (standardized) across anterior (left) and posterior (right) control embryos. Circle and triangle in
5 A & B denote a representative cell for each embryo. Scale bars = 100 microns. **C.** Standardized
6 apical surface area (black) and medial actin (red) over time in representative cells from anterior
7 (left/circle) and posterior (right/triangle). s.d. = standard deviation.

8

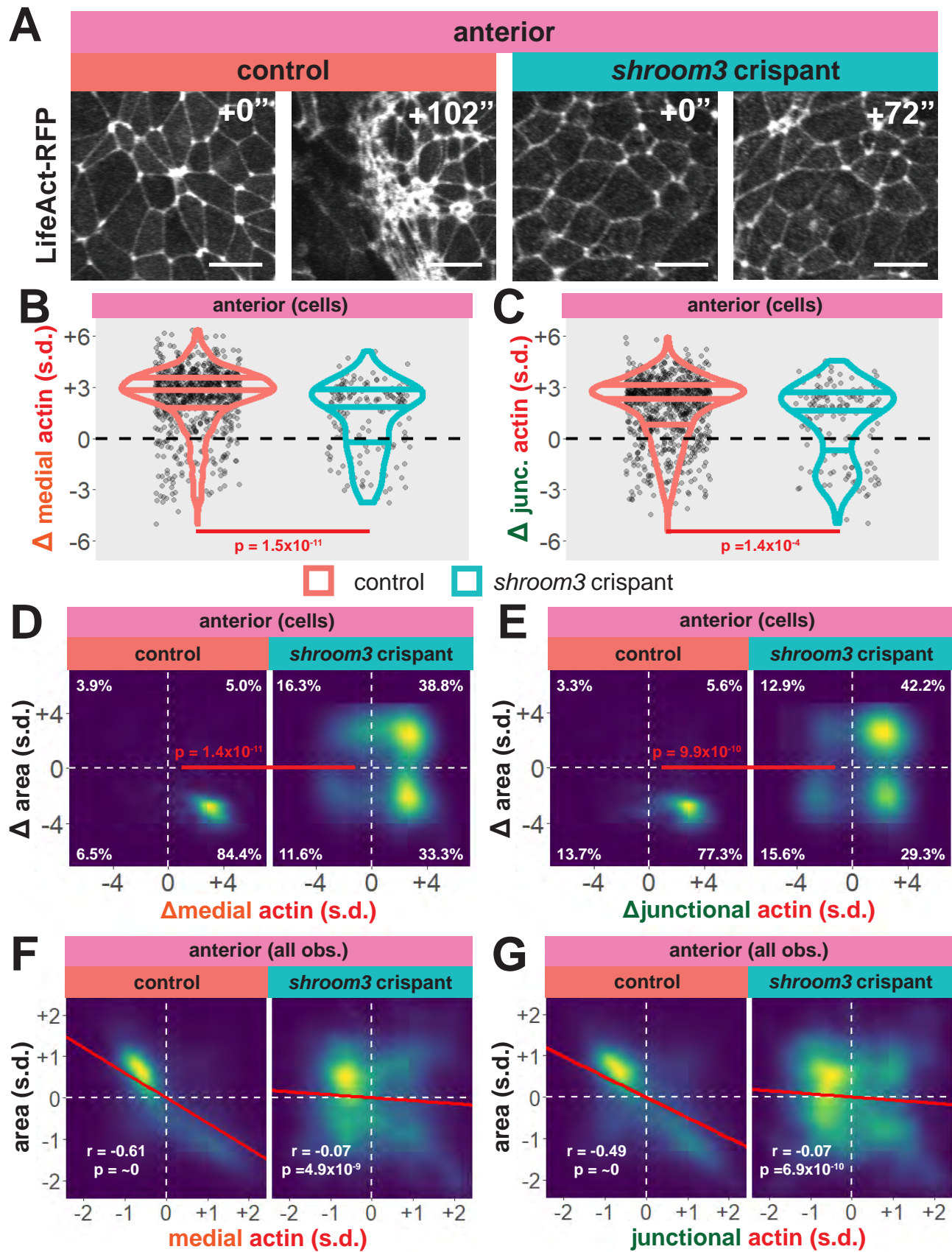


1 **Figure 3: Cells in the anterior and posterior neural ectoderm both apically constrict but**
2 **differ in their contractile protein dynamics.** Tissue-level cell size and protein localization
3 dynamics from control embryos in Figure 2. **X**. Distribution of overall change (Δ) in displayed
4 parameter (standardized) among cells from control embryos. Horizontal lines on density
5 plots/violins indicate quartiles of distribution. Black circles are individual cells. Statistical
6 comparisons performed by Kolmogorov-Smirnov (KS) test. **X'**. 2D density plots of standardized
7 variable versus time for all observations/cells in each control embryo in Figure 2. Green points
8 are measurements from the representative cells denoted in Figure 2. s.d. = standard deviation.
9



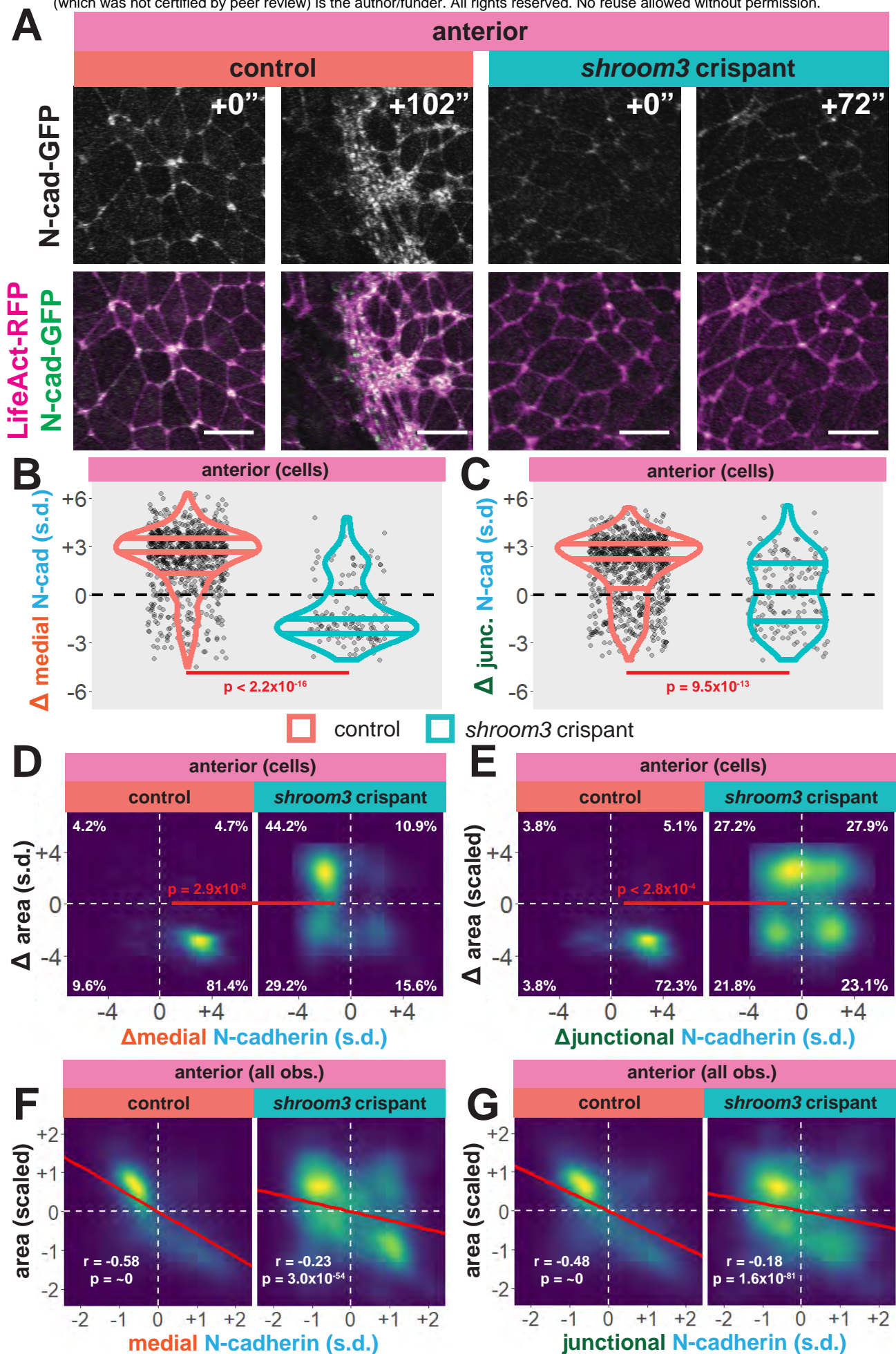
1 **Figure 4: Disruption of *shroom3* via mosaic F0 CRISPR mosaic causes differential apical**
2 **constriction phenotypes between regions of the neural ectoderm. A.** Schematic of mosaic
3 F0 CRISPR/Cas9 injections in *X. tropicalis* embryos. **B.** Workflow of identification and analysis
4 of mosaic F0 crispants. **C.** Top row, distribution of initial area (square microns) of tracked cells
5 from anterior (left) and posterior (right) embryos. Lower row, distribution of final area (square
6 microns) of tracked cells. **D.** Distribution of overall change (Δ) in apical area (standardized) from
7 all cells/embryos. In C & D, horizontal lines on density plots/violins indicate quartiles of
8 distribution. Black circles are individual cells. Statistical comparisons performed by KS test.
9 Cells situated along the mosaic interface were excluded from these analyses. s.d. = standard
10 deviation.

11



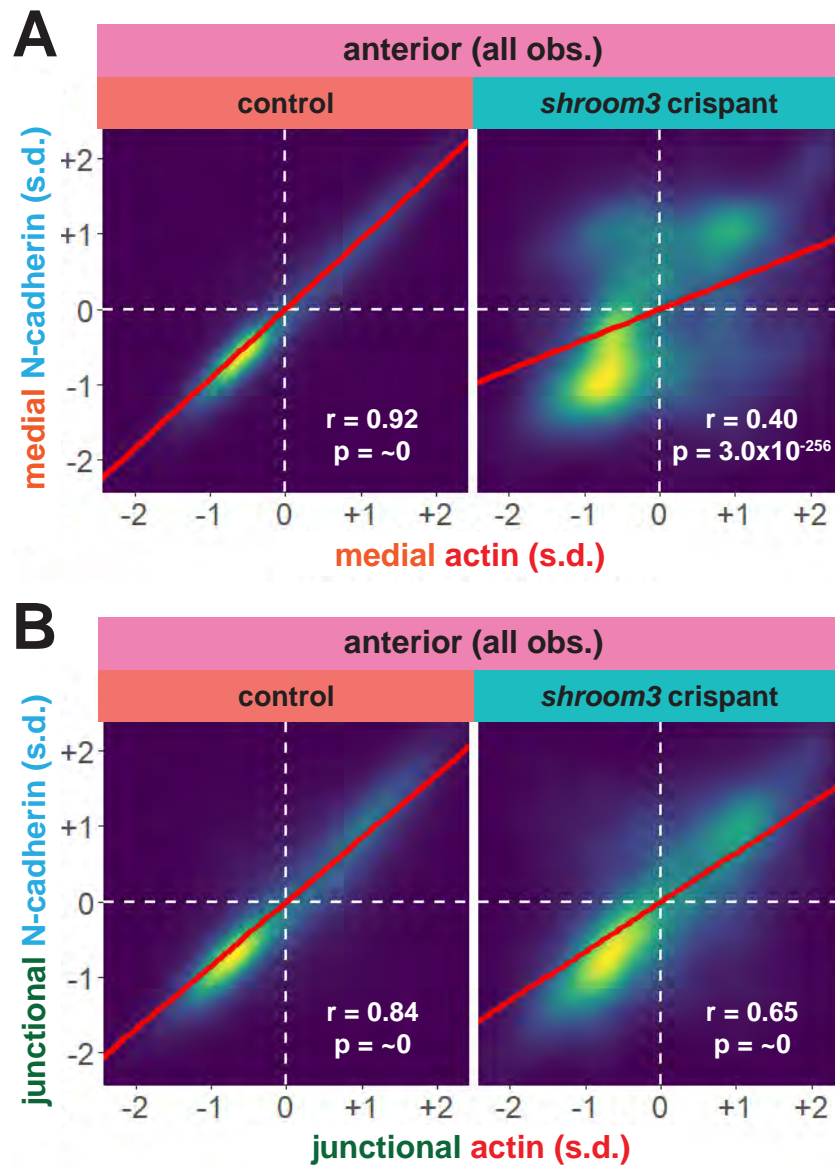
1 **Figure 5: Medial actin accumulation drives apical constriction while loss of *shroom3***
2 **disrupts actin accumulation and constriction in the anterior neural ectoderm. A.**
3 Representative images of LifeAct/actin localization in control cells (left) and *shroom3* crispant
4 cells (right) from the anterior region of the neural ectoderm. Scale bar = 15 microns. **B.**
5 Distribution of overall change (Δ) in medial LifeAct/actin (standardized) from anterior cells. **C.**
6 Distribution of overall change (Δ) in junctional LifeAct/actin (standardized) from anterior cells. In
7 B & C, horizontal lines on density plots/violins indicate quartiles of distribution, black circles are
8 individual cells, and statistical comparisons performed by KS test. **D & E.** 2D distribution of
9 changes in apical area and medial (**D**) or junctional (**E**) LifeAct/actin (both standardized).
10 Percentages in white indicate the percentage of total cells in each quadrant. Statistical
11 comparisons performed by Peacock test, a 2D implementation of the KS test. **F & G.** 2D density
12 plots of all observations of apical area versus medial (**F**) or junctional (**G**) LifeAct/actin for all
13 cells within each group. Red lines indicate best-fit line through the observations. Statistics (r
14 and p) are calculated for Pearson's correlation. Cells situated along the mosaic interface were
15 excluded from these analyses. s.d. = standard deviation.

16



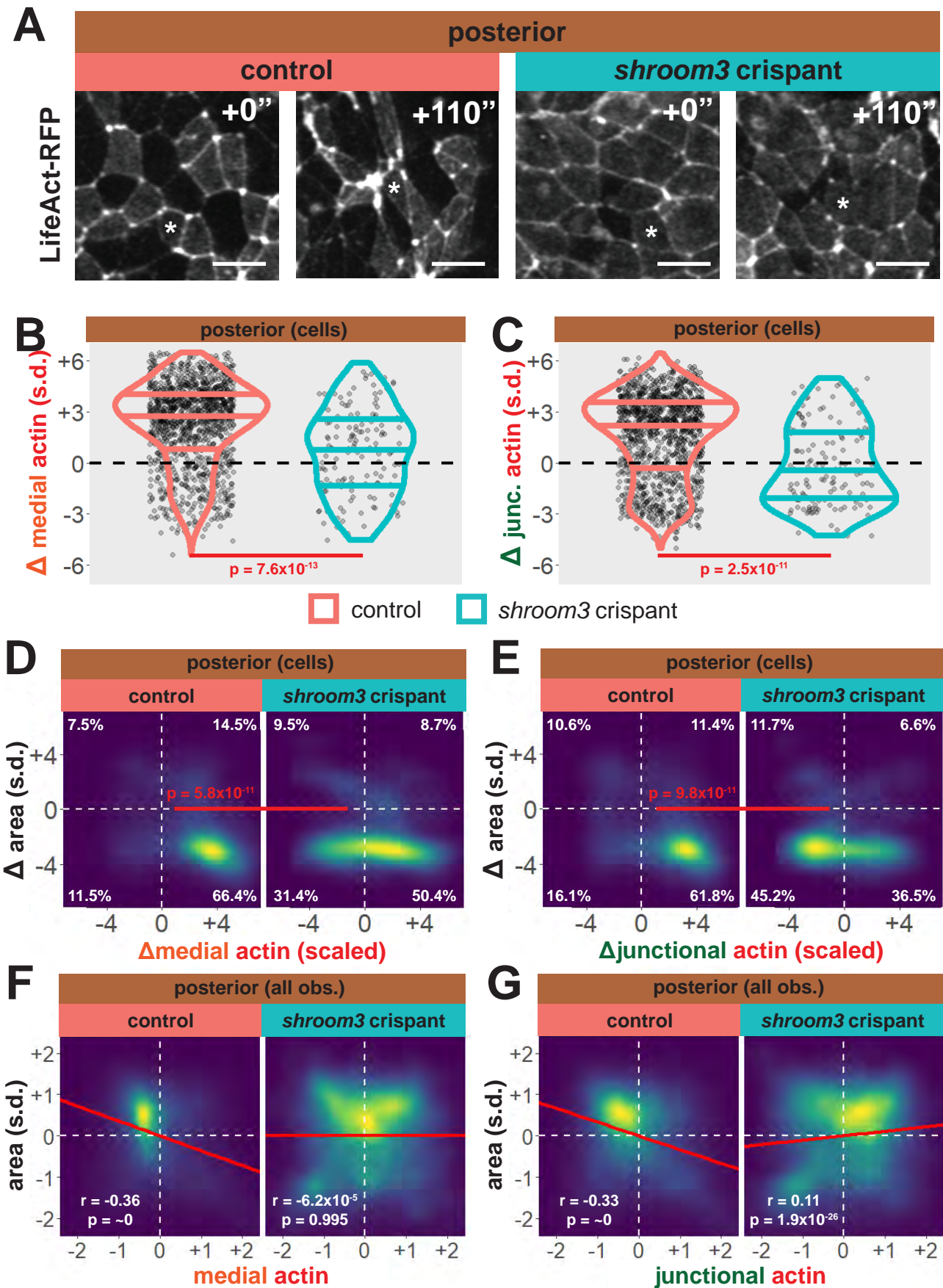
Baldwin et al. Figure 6

1 **Figure 6: Medial N-cadherin accumulation is severely disrupted in anterior *shroom3***
2 **crispant cells that fail to apically constrict. A.** Representative images of N-cadherin
3 localization in control cells (left) and *shroom3* crispant cells (right) from the anterior region of the
4 neural ectoderm. Scale bar = 15 microns. **B.** Distribution of overall change (Δ) in medial N-
5 cadherin (standardized) from anterior cells. **C.** Distribution of overall change (Δ) in junctional N-
6 cadherin (standardized) from anterior cells. In B & C, horizontal lines on density plots/violins
7 indicate quartiles of distribution, black circles are individual cells, and statistical comparisons
8 performed by KS test. **D & E,** 2D distribution of changes in apical area and medial (**D**) or
9 junctional (**E**) N-cadherin (both standardized). Percentages in white indicate the percentage of
10 total cells in each quadrant. Statistical comparisons performed by Peacock test, a 2D
11 implementation of the KS test. **F & G.** 2D density plots of all observations of apical area versus
12 medial (**F**) or junctional (**G**) N-cadherin for all cells within each group. Red lines indicate best-fit
13 line through the observations. Statistics (r and p) are calculated for Pearson's correlation. Cells
14 situated along the mosaic interface were excluded from these analyses. s.d. = standard
15 deviation.
16



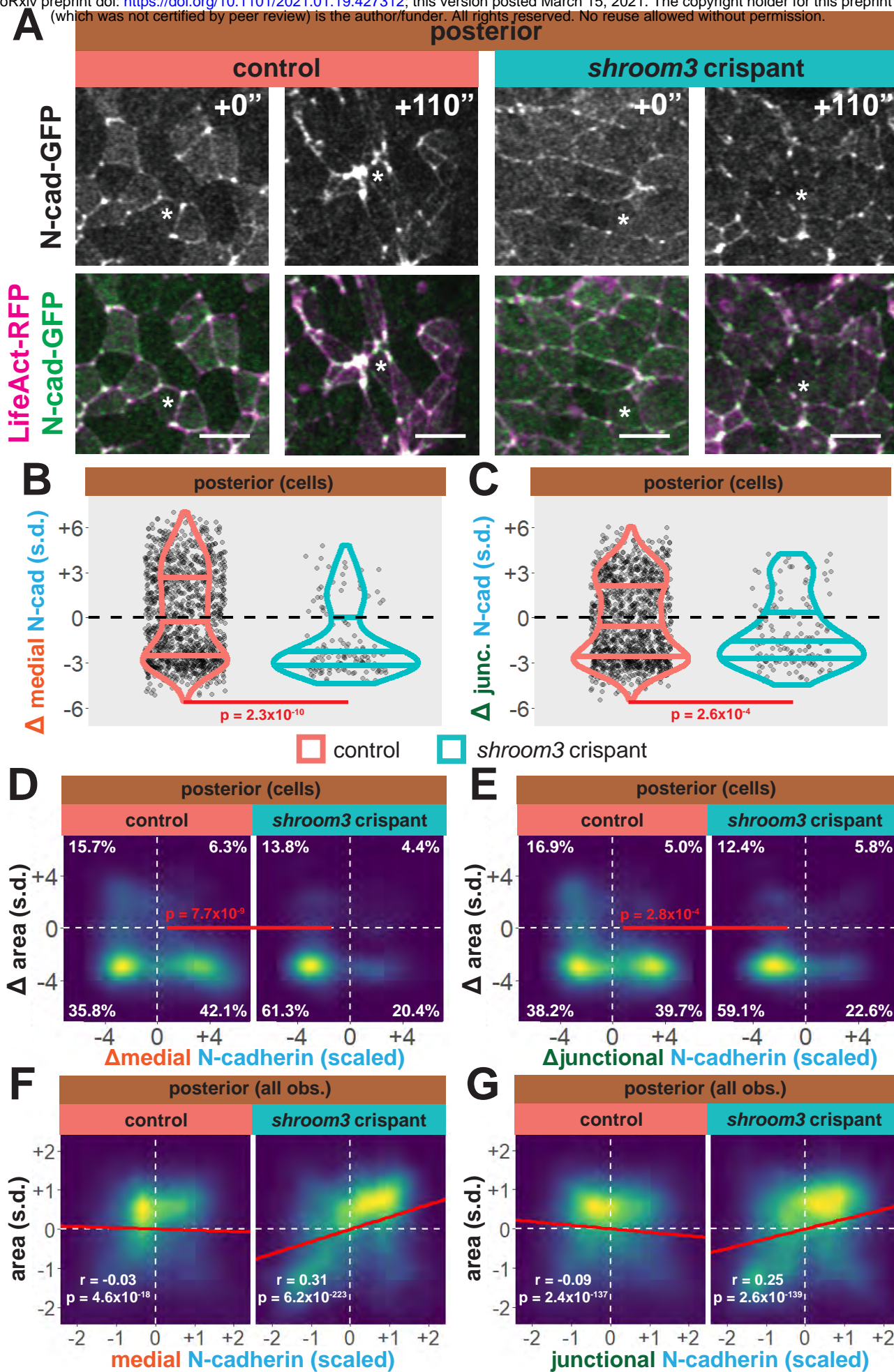
1 **Figure 7: Actin and N-cadherin accumulation are uncoupled in anterior *shroom3* crispant**
2 **cells. A & B.** 2D density plots of all observations of medial (**A**) or junctional (**B**) LifeAct/actin
3 versus N-cadherin for all cells within each group. Red lines indicate best-fit line through the
4 observations. Statistics (r and p) are calculated for Pearson's correlation. Cells situated along
5 the mosaic interface were excluded from these analyses. s.d. = standard deviation.

6



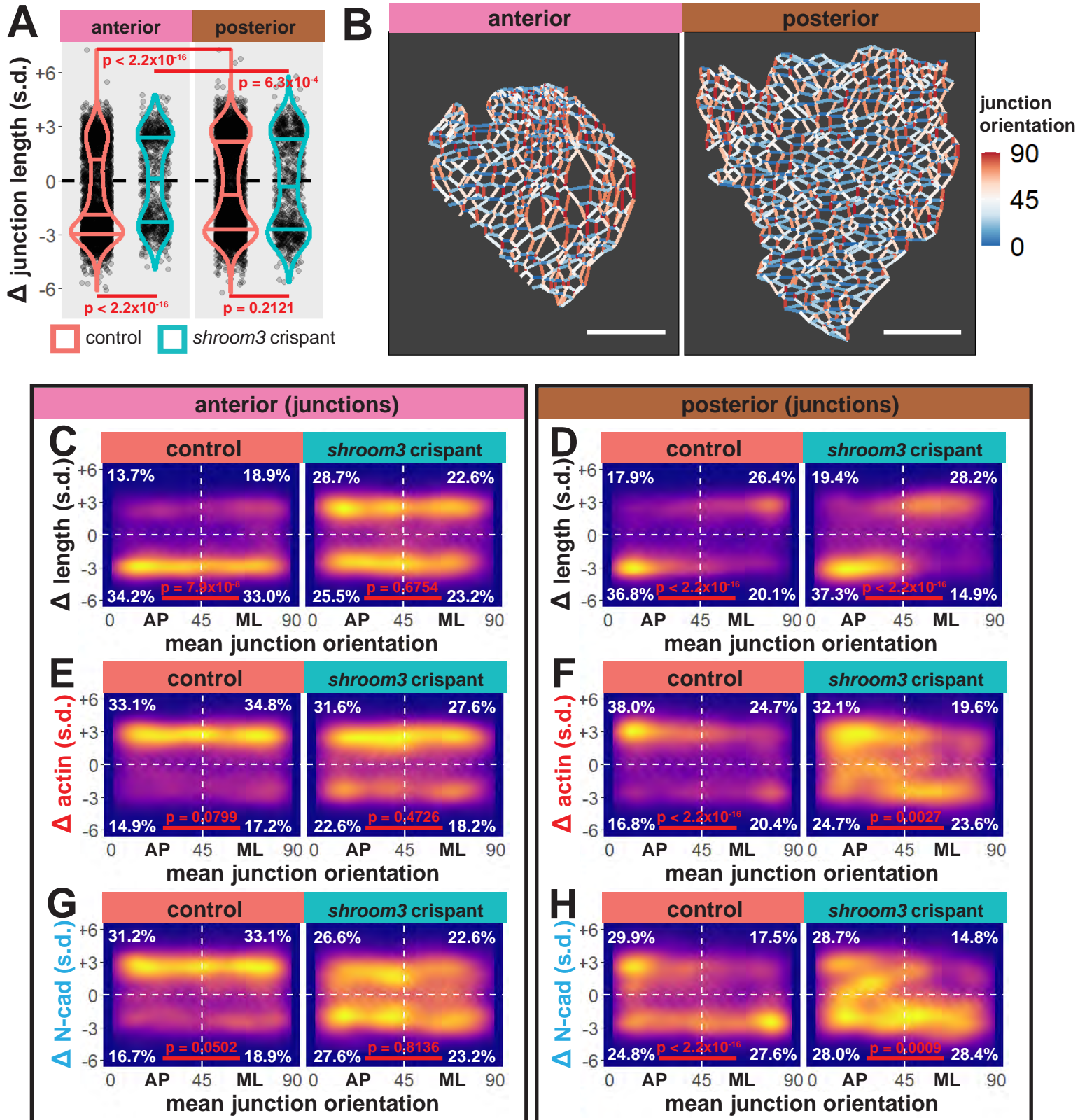
1 **Figure 8: Loss of *shroom3* disrupts actin dynamics in the posterior neural ectoderm. A.**
2 Representative images of LifeAct/actin localization in control cells (left) and *shroom3* crispant
3 cells (right) from the posterior region of the neural ectoderm. White asterisks mark the same cell
4 in each embryo. Scale bar = 15 microns. **B.** Distribution of overall change (Δ) in medial
5 LifeAct/actin (standardized) from posterior cells. **C.** Distribution of overall change (Δ) in
6 junctional LifeAct/actin (standardized) from anterior cells. In B & C, horizontal lines on density
7 plots/violins indicate quartiles of distribution, black circles are individual cells, and statistical
8 comparisons performed by KS test. **D & E.** 2D distribution of changes in apical area and medial
9 (**D**) or junctional (**E**) LifeAct/actin (both standardized). Percentages in white indicate the
10 percentage of total cells in each quadrant. Statistical comparisons performed by Peacock test, a
11 2D implementation of the KS test. **F & G.** 2D density plots of all observations of apical area
12 versus medial (**F**) or junctional (**G**) LifeAct/actin for all cells within each group. Red lines indicate
13 best-fit line through the observations. Statistics (r and p) are calculated for Pearson's
14 correlation. Cells situated along the mosaic interface were excluded from these analyses. s.d. =
15 standard deviation.

16



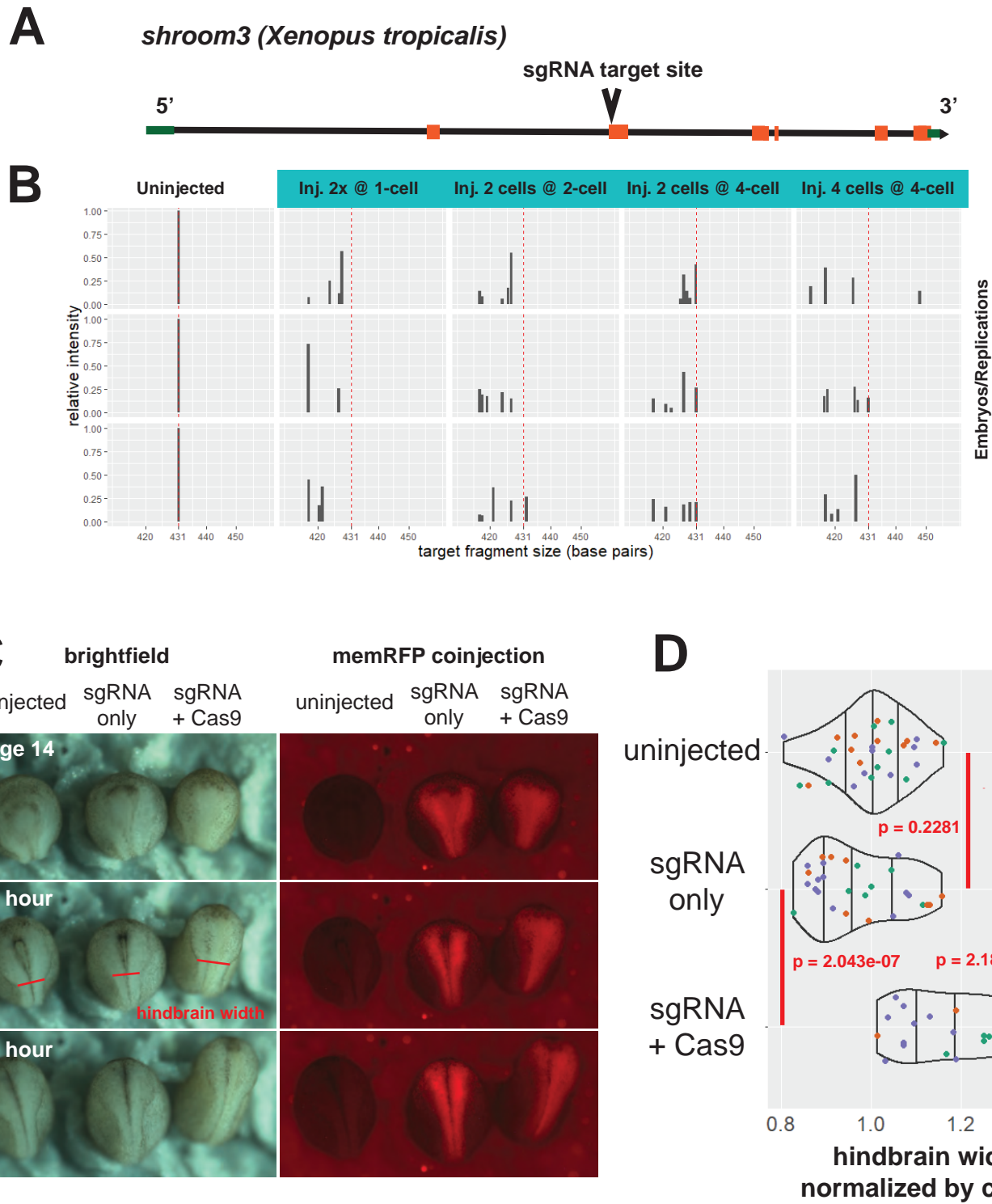
1 **Figure 9: N-cadherin dynamics are highly heterogenous in the posterior neural ectoderm**
2 **and poorly correlated with apical constriction. A.** Representative images of N-cadherin
3 localization in control cells (left) and *shroom3* crispant cells (right) from the posterior region of
4 the neural ectoderm. White asterisks mark the same cell in each embryo. Scale bar = 15
5 microns. **B.** Distribution of overall change (Δ) in medial N-cadherin (standardized) from posterior
6 cells. **C.** Distribution of overall change (Δ) in junctional N-cadherin (standardized) from posterior
7 cells. In **B** & **C**, horizontal lines on density plots/violins indicate quartiles of distribution, black
8 circles are individual cells, and statistical comparisons performed by KS test. **D & E.** 2D
9 distribution of changes in apical area and medial (**D**) or junctional (**E**) N-cadherin (both
10 standardized). Percentages in white indicate the percentage of total cells in each quadrant.
11 Statistical comparisons performed by Peacock test, a 2D implementation of the KS test. **F & G.**
12 2D density plots of all observations of apical area versus medial (**F**) or junctional (**G**) N-cadherin
13 for all cells within each group. Red lines indicate best-fit line through the observations. Statistics
14 (r and p) are calculated for Pearson's correlation. Cells situated along the mosaic interface were
15 excluded from these analyses. s.d. = standard deviation.

16



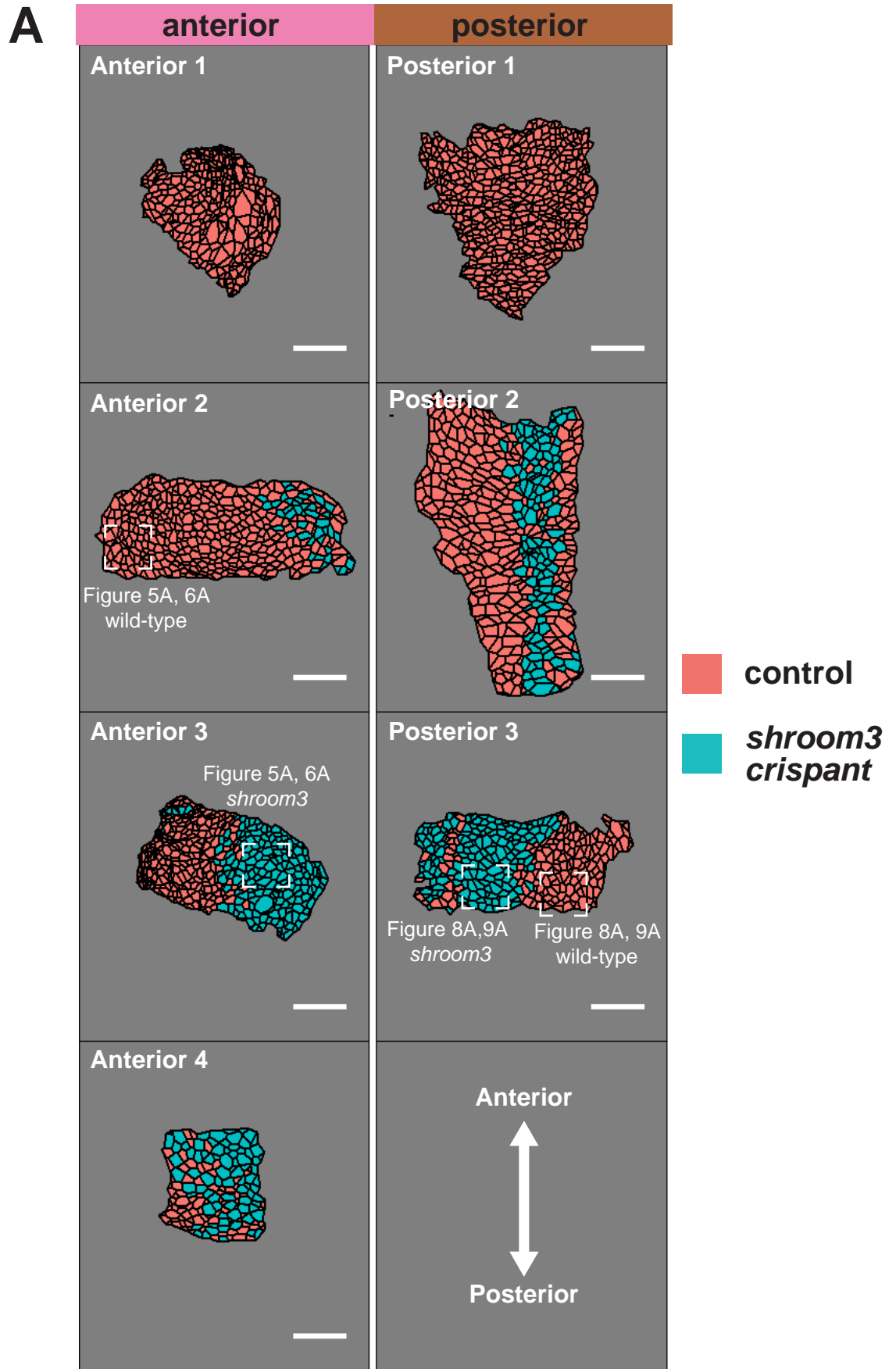
1 **Figure 10: Individual junction behaviors are more strongly polarized in the posterior**
2 **neural ectoderm. A.** Distribution of overall change (Δ) in junction length (standardized) from the
3 anterior (left) and posterior (right) regions. Horizontal lines on density plots/violins indicate
4 quartiles of distribution, black circles are individual cells, and statistical comparisons performed
5 by KS test. **B.** Junction orientation from initial frames of control embryos from Figure 2. Scale
6 bars = 100 microns. **C & D.** 2D density plots of all observations of mean junction orientation
7 over time versus overall change (Δ) in junction length (standardized) for all junctions within each
8 group. **E & F.** 2D density plots of all observations of mean junction orientation over time versus
9 overall change (Δ) in junction actin (standardized) for all junctions within each group. **G & H.** 2D
10 density plots of all observations of mean junction orientation over time versus overall change (Δ)
11 in junction N-cadherin (standardized) for all junctions within each group. Percentages in white
12 indicate the percentage of total cells in each quadrant. Statistical comparisons performed by
13 Peacock test, a 2D implementation of the KS test. s.d. = standard deviation.

14



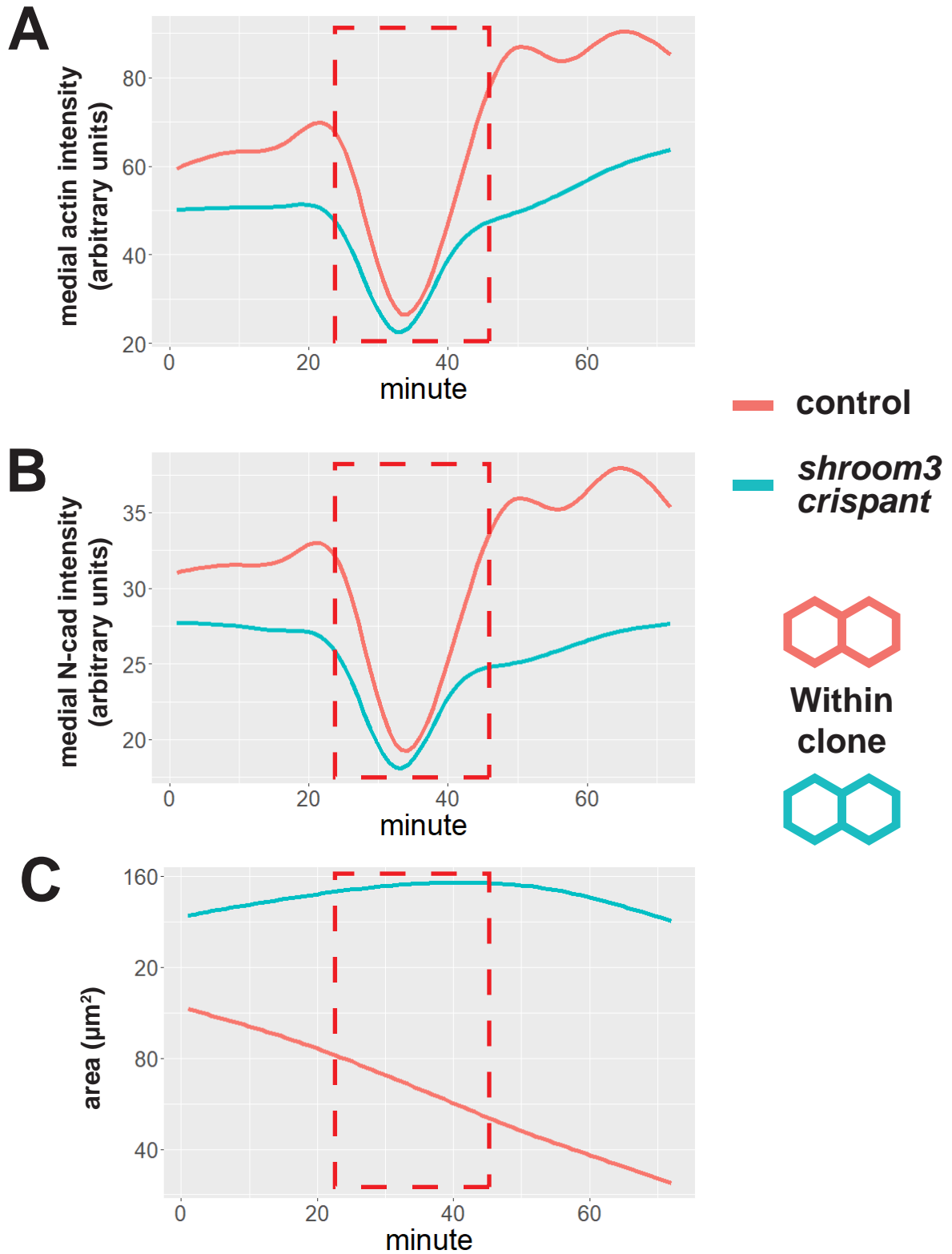
1 **Methods Appendix Figure 1: *shroom3* CRISPR validation. A.** Gene model for *shroom3* in
2 *Xenopus tropicalis* per Xenbase. The sgRNA was designed to target the 5' end of the second
3 exon. **B.** Fragment analysis to validate efficacy of sgRNA + Cas9 injections. A 431 base pair
4 genomic fragment of *shroom3* at the sgRNA target site was generated by PCR from whole
5 embryo lysates and subjected to capillary electrophoresis. Uninjected embryos that did not
6 receive CRISPR reagents showed one band at 431 base pairs (left column, red dashed line).
7 Embryos injected with *shroom3* sgRNA + Cas9 protein at various times and frequencies are
8 displayed in right-hand columns, with the wild-type fragment size indicated by the red dashed
9 line. Relative frequency of wild-type *shroom3* fragment size is severely reduced in injected
10 embryos. Each plot represents one embryo. **C.** sgRNA controls. Embryos were injected with
11 *shroom3* sgRNA alone or sgRNA plus Cas9 protein into the dorsal blastomere at the 8-cell
12 stage, as in the imaging experiments. membrane-RFP mRNA was used as injection/lineage
13 tracer. Red line segments indicate the posterior boundary of the hindbrain, which was used to
14 calculate values in D. **D.** Quantification of sgRNA controls. Hindbrain widths were measured at
15 approximately stage 17 as indicated in C. Colors of individual points indicate clutch membership
16 of each embryo. An average width of the hindbrain of uninjected embryos of each clutch was
17 calculated, then all embryos in each clutch had their hindbrain width calculated as a ratio of that
18 average. Density distribution violins were then calculated based on pooled clutches. Vertical
19 lines on density plots/violins indicate quartiles of distribution. Statistical tests were calculated
20 using T-test.

21

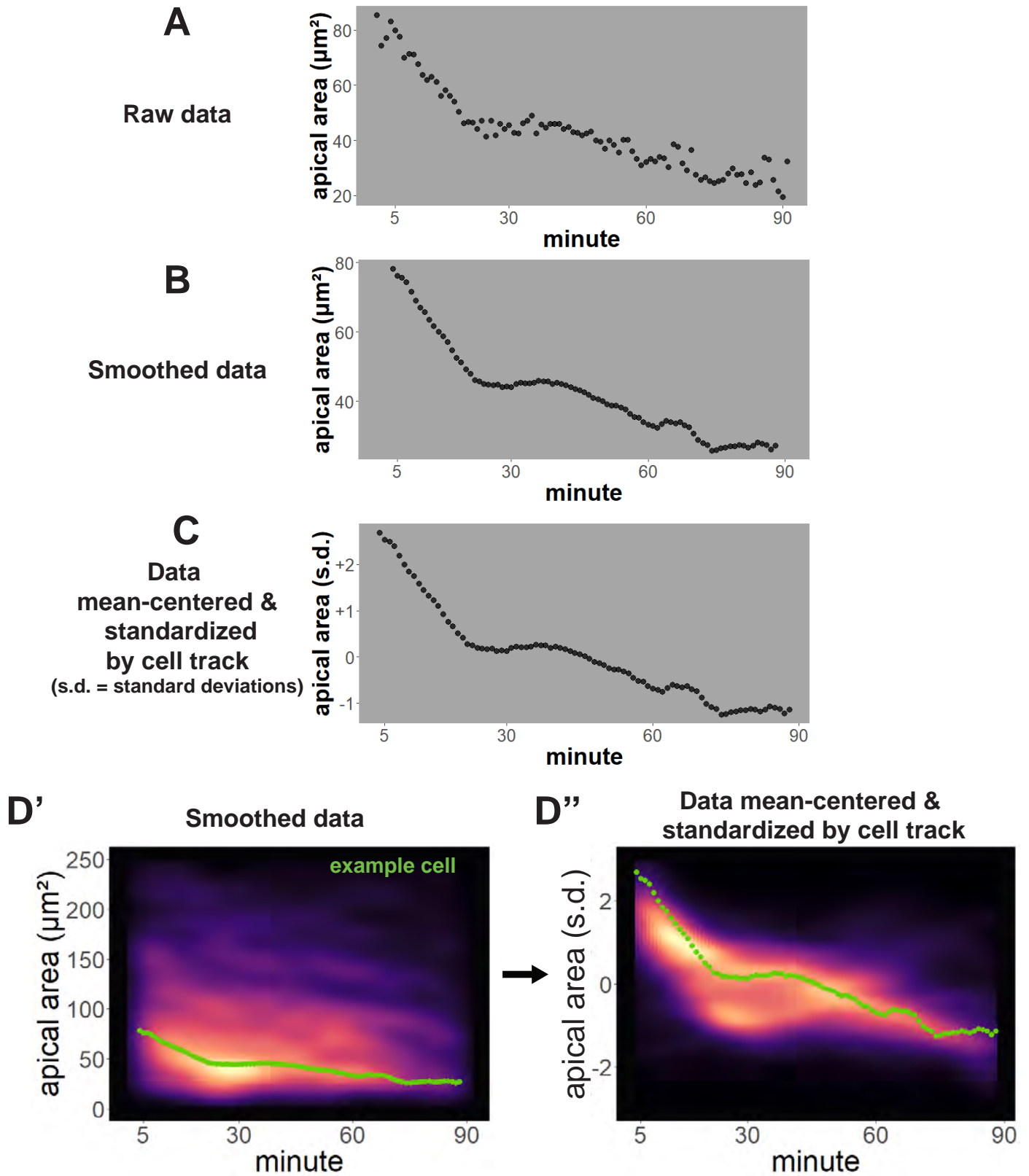


1 **Methods Appendix Figure 2: Maps of initial frames and *shroom3* crispant calls for each**
2 **analyzed embryo.** Representative cells in Figures 5, 6, 8, & 9 are highlighted. Scale bar = 100
3 microns.

4



1 **Methods Appendix Figure 3: Fluorescent aberration in an anterior-imaged embryo. A.**
2 Smoothed mean of medial LifeAct-RFP/actin fluorescent intensity across all imaged cells across
3 time. **B.** Smoothed mean of medial N-cadherin-GFP fluorescent intensity across all imaged cells
4 across time. **C.** Smoothed mean of apical surface area across all imaged cells across time. Red
5 dashed box indicates frames where fluorescence values dropped temporarily. Cells were
6 tracked through these frames, but the frames were removed from analysis of this embryo.
7



1 **Methods Appendix Figure 4: Per-cell data processing and analysis. A.** Raw data for apical
2 area (converted to square microns) of an individual cell over time. **B.** Apical area
3 averaged/smoothed over 7 frames. **C.** Smoothed data after mean-centering and
4 standardization. **D'**. Apical area (square microns) versus time of all cells from a control embryo
5 displayed as a density plot. The green dots are from the same cell as displayed in B. **D''**. The
6 same cells as D' after mean-centering and standardization of each cell track. The green dots
7 are from the same cell as displayed in C. s.d. = standard deviations.

8